氧化鋅薄膜之雙軸向應變效應與光學增益之研究

研究生：李宜錦　　指導老師：謝文峰　教授

國立交通大學光電工程研究所

摘要

為了研究氧化鋅薄膜和基板之間的應力，我們成長氧化鋅薄膜在三種不同的基板：藍寶石基板(001)面、矽(111)面與碳化矽(001)面。接著用波長 355nm 的三倍頻 Nd:YVO_4 雷射激發磊晶品質佳的氧化鋅薄膜，量測其光學增益值。從反射式高能電子繞射圖及 X 光繞射ω–rocking curve 掃描中，我們發現成長在藍寶石基板和碳化矽基板上的氧化鋅薄膜品質較佳。我們也針對成長在藍寶石基板和碳化矽基板上的氧化鋅薄膜(202)面，做 X 光繞射ϕ-scan 掃描，清楚的發現其具有六重對稱，確定為磊晶薄膜。至於成長在矽(111)面的氧化鋅薄膜，並沒有發現六重對稱。利用 X 光繞射對氧化鋅薄膜 (002) 和 (110)面做ω-2θ掃描，我們決定三種樣品的氧化鋅薄膜 *c* 軸與 *a* 軸的晶格常數。配合室溫光激光光譜的分析，分析出氧化鋅薄膜和三種基板間的雙軸向應變效應。除了晶格常數匹配的影響，熱膨脹效應其實也影響著薄膜和基板間的應力。

此外，我們也量測了生長於藍寶石基板的氧化鋅薄膜上在不同激發強度下的光學增益值。發現雷射激發強度在 4.585MW/cm^2 時，氧化鋅薄膜的激發輻射主是來自於激子與激子間的非彈性碰撞。當雷射激發強度達到 8.45MW/cm^2 時，激子的數目會增加，激子間不再有庫倫作用力，而形成電子電洞的電漿態。當雷射激發強度達到 25.3MW/cm^2，這時候的最大光學增益值是 187 cm^{-1}。隨著雷射激發強度的增加，氧化鋅薄膜的激發輻射將會逐漸由電子電洞形成的電漿態產生。

Effect of Biaxial Stress on ZnO Thin Films and in-Plane Optical Gain

Student: Yi-Chin Lee. Advisor: Prof. Wen-Feng Hsieh

Institute of Electro-Optical Engineering

College of Electrical Engineering and Computer Science

National Chiao Tung University

Abstract

We study the effect of biaxial stress on the ZnO thin films by growing those onto Al_2O_3 (001), Si (111) and SiC (001). We use a third harmonic of Nd:YVO_4 laser (λ=355nm) to measure the in-plane optical gain of high-quality ZnO epilayers on Al_2O_3. From reflection high energy electron diffraction (RHEED) observation and ω–rocking curve, we found qualities of ZnO/Al_2O_3 and ZnO/SiC are better. Phi scans for (202) peaks of three samples indicate six-fold symmetry and epitaxial growth of ZnO thin films onto Al_2O_3 and SiC except Si (111). We have investigated X-ray ω-2θ scan for (002) and (110) reflections to determine *c*- and *a*-axis lattice constants of ZnO thin films on different substrates. With room-temperature (RT) PL spectra of three samples, we can derive the stress states in films. The thermal stress can also play a key role in deciding the residual strain in film.

Beside we found that the inelastic exciton-exciton (ex-ex) scattering dominantly contributes to the optical gain at excitation densities, 4.585 MW/cm^2 and the electron-hole plasma (EHP) state at excitation densities, 8.45MW/cm^2. Maximum gain of 187 cm^{-1} at the excitation density of 25.3 MW/cm^2 is obtained. With increasing excitation, density contribution from the EHP state gradually takes over at the lower energy side in the optical gain spectrum.

致謝

呼!終於來到了最感性的一刻。我現在的心情，彷彿一個入圍好幾屆金曲獎的歌手，最後終於拿著獎座，站上舞台，心中百感交集，不知道該說什麼是好。

回顧碩士班這兩年，一路上有許多人幫助我、照顧我。首先，要感謝國科會計畫編號 NSC 92-2112-M009-037 的經費支持，使得本研究得以順利完成。再來感謝謝文峰老師，不論在學業上或者球技上(桌球)，都盡心盡力的教導我，讓我獲益良多。再來是材料組的老大－阿政學長。每次實驗上遇到困難，去找學長，學長都會先抓抓他的捲髮，沉思了幾分鐘，然後一拍大腿，大叫：「有了！」就一一替我解決困難。雖然有時候學長對我是『恨鐵不成鋼』，很嚴格，可是我知道學長是為我好，真的很感激！

再來是材料組其他的學長，蔡老大、維仁和黃董，謝謝你們在我剛接下 L-MBE 的時候，一直幫助我解決水、電和儀器的問題。沒有你們，L-MBE 可能會掛在我手上。蔡老大學長，雖然我們只相處半年，但是我發現在你看似凶惡的小平頭下，其實是很平易近人的。還有碩一帶我的弘裕學長，謝謝你的筆記和考古題，讓我生平第一次拿到書卷獎。我會永遠記得你對我的好。還有感謝即將進來實驗室的鄭信民學長，因為你的拔刀相助，讓我的論文又再多了幾頁。

再來是實驗室其他的學長姐，家弘、晴如、智章、小戴、奎哥和奶油，謝謝你們一直都得忍受我無來由的人來瘋，還有給予我實驗上或生活上的幫助。希望家弘學長可以趕快找到另一半，吹奏陶笛的技巧越來越好。

再來是感謝我的材料組同學，楊松。每次遇到問題，都會不辭辛勞的幫助我，希望你能夠很快的從博士班畢業，然後縱橫股票界賺大錢。還有少根筋但是很貼心的映如，很欠扁但還蠻有趣的英仁，善良的史來姆，喜歡小貓的佩芳，我的同居密友依娜，對面液晶實驗室的全體同學，美琪、品發、美津和小伍，我的愛漂亮高中同學玉棉，愛裝可愛的偉志，越來越年輕的美杏，謝謝你們陪我在碩士兩年裡，吃喝玩樂，有空到我家來坐坐。

再來是實驗室的學弟妹，俊毅、國峰、盈秀、小豪、文勛和家斌，實驗室有你們的加入，變得有活力不少。尤其俊毅和國峰在實驗上也給予我許多幫忙，讓我呼來喚去，分擔了許多事情，謝謝你們。當然還少不了兩個大學專題生，明容和穎書學妹，每次看到你們，我的心情都會很愉快。

最後感謝我的爸爸和媽媽，給予我一個良好的學習環境，讓我可以順利的完成學業。我妹我姐的支持，聽我吐苦水，謝謝！

時光飛逝，歲月如梭，我終於要畢業了。離開了實驗室，也離開了待了六年的交大。希望實驗室的每個人，離開了實驗室的時候，都能夠滿載著收穫，喜悅的離開。

Contents

Chinese Abstract ……–i-

English Abstract .....……–ii-

Acknowledgements ……...-iii-

Contents ……-iv-

List of Figures ……..-vii-

List of Tables ……-ix-

Chapter 1 Introduction ……...- 1 -

1.1 Motivation ……...- 2 -

1.2 Organization of the thesis ……...- 3 -

Chapter 2 Theoretical background ……..- 4 -

2.1 A brief review of structure and photoluminescence property of ZnO …..……...- 4 -

2.1.1 Structure ……...- 4 -

2.1.2 Photoluminescence property ……...- 5 -

2.2 The principle of Laser-MBE deposition ……...- 6 -

2.3 Reflection High Energy Electron Diffraction ……...- 7 -

2.4 X-ray diffraction ……- 11 -

2. 5 Photoluminescence characterization ……..- 11 -

2.5.1 Photoluminescence property ……- 11 -

2.5.2 Stimulated emission and optical gain ……- 13 -

Chapter 3 Experimental detail ……- 15 -

3.1 The growth of the ZnO films ……- 15 -

3.1.1 The Laser-MBE system Layout ……- 15 -

3.1.2 Target preparation ……- 16 -

3.1.3 The surface treatment of the substrate ……- 16 -

3.1.4 Operating process of the Laser-MBE system ……- 17 -

3.2 Determination of structures and synthesis of the ZnO thin films .- 18 -

3.2.1 X-ray diffraction ……- 19 -

3.3 Measurements of optical properties ……- 19 -

3.3.1 Photoluminescence detection system ……- 19 -

3.3.2 Stimulated emission and optical gain detection system .- 20 -

3.3.3 Optical gain measurement ……- 21 -

Chapter 4 Results and Discussion ……- 23 -

4.1 Crystalline quality of the ZnO thin films on different substrates .- 23 -

4.1.1 RHEED observation ……- 24 -

4.1.2 XRD ω–-rocking curve ……- 27 -

4.1.3 Phi Scan ……- 28 -

4.2 Effect of Biaxial Strain on ZnO Thin Films ……- 31 -

4.2.1 Lattice determination by XRD ω-2θ scan ……- 31 -

4.2.2 Photoluminescence spectra ……- 35 -

4.3 Stimulated emission and Optical gain in ZnO epilayers ……- 40 -

4.3.1 Photoluminescence spectra with Nd: YVO_4 laser under various excitation densities at RT……- 40 -

4.3.2 Stimulated emission spectra for various excitation stripe lengths at RT……- 44 -

Chapter 5 Conclusion and Perspective ……...- 50 -

5.1 Conclusions ……- 50 -

5.2 Perspective ……- 50 -

References ……- 52 -

List of Figures

Fig. 2-3 Schematic diagram of the RHEED geometry ……..- 9 -

Fig. 2-4 Ewald sphere construction and diffraction geometry of RHEED …..- 10 -

Fig. 2-5 Visualization of (a) an exciton bound to an ionized donor, (b) a neutral donor, and (c) a neutral acceptor ……- 12 -

Fig. 2-6 Dispersion curves for polaritons (dotted line) and free excitons and photons (solid lines) ……- 13 -

Fig. 2-7 Schematic representations of various interaction processes of light with matter namely ……- 14 -

Fig. 3-2 XRD ω–2θ scans geometry of ZnO (A) (002) and (B)(1 1 0) diffraction peaks……- 19 -

Fig. 4-1 RHEED patterns of (a) the Al_2O_3 substrate and (b) the ZnO epilayers along [2-1-10] and [1-100] azimuths. ……- 24 -

Fig. 4-2 Schematic diagram shows the epitaxial relationship of ZnO (0001) grown on *c*-plane Al_2O_3. ……- 25 -

Fig. 4-3 RHEED patterns of (a) *c*-plane Al_2O_3[1-100], (c) Si(111) and (e) SiC substrate and ZnO thin films on above mentioned substrates. ……..- 26 -

Fig. 4-4 Intensity profiles of RHEED patterns of ZnO thin films on *c*-plane Al_2O_3 along [1-100] azimuth…….. - 26 -

Fig. 4-5 A set of ω̃–rocking curve of the ZnO (002) peak on (a) Al_2O_3 (b) Si (111) (c) SiC substrates…….. - 29 -

Fig. 4-6 A set of in-plane ϕ scan of the ZnO thin films (202) and the substrates (202) peak. (a) Al_2O_3; ZnO/Al_2O_3 (b) Si (111); ZnO/Si(111) (c) SiC; ZnO/SiC…… - 30 -

Fig. 4-7 XRD ω–2θ scan (002) of the ZnO/Al_2O_3, ZnO/Si (111) and ZnO/SiC samples…… - 33 -

Fig. 4-8 XRD ω–2θ scan (110) peak of the ZnO/ Al_2O_3, ZnO/Si (111) and ZnO/SiC samples…… - 34 -

Fig. 4-9 Length of the *a*-axis is plotted against the length of the *c*-axis for the ZnO thin films grown on Al_2O_3, Si (111) and SiC……... - 35 -

Fig. 4-10 Emission spectra of the ZnO thin films on Al_2O_3 in the temperature range 10-300K…….. - 36 -

Fig. 4-11 The RT PL spectra of the ZnO/Al_2O_3, ZnO/Si (111) and ZnO/SiC samples ..……- 38 -

Fig. 4-12 Exciton energies of ZnO layers as a function of strain along the *a* axis are plotted……..…….. - 39 -

Fig. 4-13 The inset shows the method by which the crystal is excited and the amplified light (I_o) is detected…… - 41 -

Fig. 4-14 RT PL spectra under various excitation densities show the inelastic ex-ex scattering induced stimulated emission…...…… - 41 -

Fig. 4-15 The spectral emission intensity versus the excitation density for (a) the inelastic ex-ex scattering (b) the EHP state……...…… - 42 -

Fig. 4-16 Stimulated emission spectra for various excitation stripe lengths at RT. I_{pump}= (A) 9.19 MW/cm^2 (B) 25.3MW/cm^2 ……- 46 -

Fig.4-17 absorption coefficient versus photon energy for good quality (α) and poor quality of ZnO thin films (α')..…… - 47 -

Fig. 4-18 A set of the variation of light output with length of excited region for excitation density=25.3 MW/cm^2. ……- 48 -

Fig. 4-19 Optical gain spectrum of a ZnO epilayer under various excitation density at RT ……..……- 49 -

List of Tables

Table 2-1 Some characteristic parameters of ZnO and the substrates used for its growth ..... - 5 -

Table 3-1 LPX210i (KrF) Specifications .....- 16 -

Chapter 1
Introduction

Wurtzitic ZnO is a wide-bandgap (3.437 eV at 2 K) [1] semiconductor with a high melting temperature which has many applications, such as piezoelectric transducers, varistors, phosphors, and transparent conducting films. Most of these applications require only polycrystalline material; however, recent successes in producing large-area single crystals have opened up the possibility of producing blue and white light emitters, and high-temperature, high-power transistors. The main advantage of ZnO as a light emitter is its large exciton binding energy (60 meV). For electronic applications, its attractiveness lies in having high breakdown strength, high saturation velocity, and optical UV lasing, at both low and high temperatures, which has already been demonstrated [2],[3]. Although efficient electrical lasing must await the further development of good, p-type material, ZnO is also much more resistant to radiation damage than other common semiconductor materials such as Si, GaAs, CdS, and even GaN; thus, it should be useful for space applications [4]. In contrast to technical limitations of GaN, excitons of ZnO material are stable even at elevated temperatures due to its largest exciton binding energy in the semiconductor family. It is expected that exciton as well as polariton lasers will be fabricated using the ZnO-related materials by overwhelming the GaN [5] in the near future. However, there are two big challenges for device fabrication using the ZnO material: (i) control of *p*-type conductivity and (ii) higher crystalline quality. Considering the *p*-type ZnO, much literature has recently been reported on the *p*-*n* homojunction with rectification properties, although reproducibility is still under the investigation.

Recently, progresses in ZnO heteroepitaxy with either plasma-assisted

molecular-beam epitaxy (P-MBE) [6],[7] or pulsed laser deposition (PLD) [8] have led to high-quality ZnO epilayers. Optically pumped stimulated emission and lasing have been demonstrated at RT [2],[3]. However, investigations on lasing mechanisms showed discrepancy in different reports. P. Yu and co-workers observed optically pumped lasing in a 55 nm thick microcrystalline ZnO film grown on Al_2O_3 (0001) by PLD [9]. The lasing mechanism was attributed to inelastic exciton-exciton (ex-ex) scattering and a peak gain of 320cm^{-1} was observed at a fluence of 3.0 $\mu J/cm^{-2}$ [2],[7].

In our previous study, we have fabricated ZnO epitaxial films under high vacuum ambiance without extra oxygen by laser molecular-beam epitaxy (Laser-MBE) [10]. The full width at half maximum (FWHM) of double-crystal X-ray diffraction (002) peak for ZnO thin films on Al_2O_3 is 299 arcsec. Under such high vacuum ambiance (base pressure=1x10^{-9} torr), we can easily use RHEED to *in-situ* monitor the growth evolution of the ZnO thin films.

1.1 Motivation

The knowledge of strain or stress state in epitaxial ZnO is very important for better understanding film's property and ZnO-based devices. However, there are few correlative reports [11],[12]. Biaxial strain in the epitaxial layer and the substrate is induced by the larger lattice mismatch and the different thermal expansion coefficients between the epilayer and substrate. In this study, we grew ZnO thin films on three different substrates [Al_2O_3, Si (111) and SiC] to observe the biaxial strain between the ZnO epilayer and the substrate. Al_2O_3 is a frequently used substrate for growing ZnO thin film. Si (111) is cheap and convenient. SiC has

smaller lattice mismatch (5%) to the ZnO thin films.

Different optical pumping conditions could be a reason for the observed discrepancy; the different crystal properties of the investigated epilayers should also play a critical role in lasing mechanisms. Large amount of grain boundaries in the sample provide additional internal reflection of the emission light. These effects may facilitate the lasing with excitonic processes. The structural defects result in numerous optical losses and thus a high threshold [13]. Thus, in the later part, we choose good crystalline quality sample (ZnO thin films on Al_2O_3) and record the in-plane optical gain with the RT emission spectrum.

1.2 Organization of the thesis

The thesis consists of five chapters, including the present introduction. We introduce the background mechanisms of Laser-MBE as well as the basic theory of some characterization tools of semiconductor such as *in-situ* RHEED observation, X-Ray Diffraction (XRD), ϕ scan and photoluminescence (PL) spectroscopy. In chapter 3, we describe the experimental details, including the sample preparation, the equipment setups and parameters of characterization. The optical properties of the ZnO thin films are presented in chapter 4. By growing ZnO thin films on different substrates, we study the effect of biaxial stain in the ZnO epilayers and substrates, heterointerfaces. Later, we choose high quality ZnO films to excite exciton radiation and measure the optical gain of the ZnO films. In the final chapter, we conclude our investigations on the ZnO thin films and propose some topics for further study.

Chapter 2
Theoretical background

2.1 A brief review of structure and photoluminescence property of ZnO

2.1.1 Structure

Fig. 2-1 shows the wurtzite structure of the ZnO crystal. ZnO is a crystal of hexagonal structure with the lattice constant of *a*=3.249 Å, *c*=5.207 Å. The deposited thin films usually have *c*-axis-oriented textures.

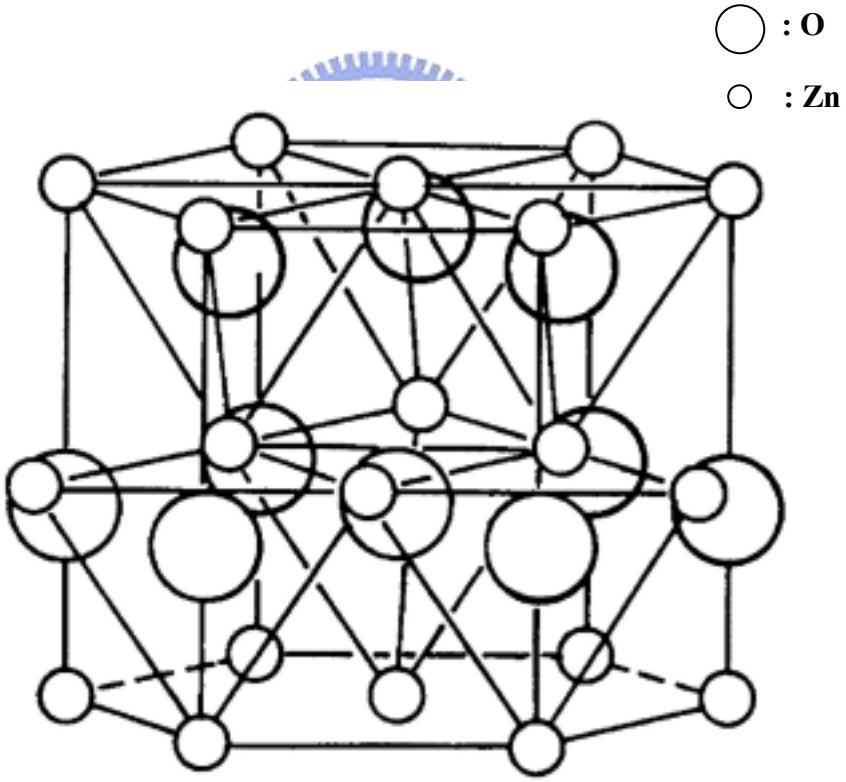

Fig. 2-1 Wurtzite structure

The crystalline properties of the ZnO layers are poor, especially for the large lattice mismatch between the epilayers and the substrates. It is noted that the ZnO layers grow normally on the Al_2O_3 substrate under the lattice mismatch ($\triangle a/a_o$) of

~18%. This large lattice mismatch, together with the different thermal expansion coefficients between the epilayers and the substrate, induces the biaxial strain in the epitaxial layers. Some properties of usually used substrates for the ZnO thin films was listed in the Table 2-1.

Table 2-1 Some characteristic parameters of ZnO and the substrates used for its growth

Crystal	Lattice[14]			Thermal Expansion Coefficient[10^{-6}/K]	
	Type	a(Å)	c(Å)	*a* axis	*c* axis
ZnO	Hexagonal (Wurtzite)	3.249	5.207	4.75[15]	2.9[15]
Al_2O_3(001)	Hexagonal (Wurtzite)	4.758	12.99	7.5	8.5
Si(111)	Diamond Cubic	3.84	…	3.59	…
6H-SiC (001)	Hexagonal (sphalerite)	3.081	15.117	4.2	4.68

2.1.2 Photoluminescence property

Wide band gap semiconductors have attracted a great deal of attention because of the ever-increasing commercial desire for short wavelength light emitting devices. Among a few candidates, ZnO has a direct band gap of 3.37 eV at RT and a large exciton binding energy of 60 meV, which in principle allows the exciton governed luminescence at short wavelength to be dominant at RT. Recent developments in MBE technique or PLD have led to high-quality ZnO epilayers.

2.2 The principle of Laser-MBE deposition

The inner of the deposition chamber was shown as Fig. 2-2. The physics of the laser material-deposition process had been investigated in detail that included the evaporation of the target material, the formation of a high-temperature plasma due to the absorption of laser energy by the evaporated material, and the expansion of the plasma resulting in the deposition of the thin films. Depending on the types of interaction of the laser beam with the target, the laser deposition process can be classified into three regimes:

i. Interaction of the laser beam with the target

At high power densities obtained from nanosecond excimer-laser pulses, heating and evaporation of the material will occur at the beginning of the laser pulse. The amount of evaporated flux varies linearly with the pulse energy density.

ii. Interaction of the laser beam with the evaporated material

As the evaporated material is further heated by the interaction of the laser beam, it results in the formation of high-temperature plasma consisting of ions, atoms, molecules, electrons, etc. The temperature attained by the plasma depends on the power density, frequency, pulse duration of the laser beam, and the optical and thermo physical propertied of the material. During the incidence of the laser pulse, the isothermal expanding plasma is constantly augmented at its inner surface with evaporated particle from the target. The acceleration and the expansion velocities in the regime are found to depend upon the initial velocity of plasma. Because of the large lateral dimensions of the plasma, it expands preferentially normal to the irradiated surface.

iii. Adiabatic plasma expansion and the deposition of the thin films

After the termination of the laser pulse, this plasma expands adiabatically with the expansion velocities controlled by its initial dimensions. The plasma cools rapidly during the expansion process, with the edge velocities reaching asymptotic values. The particles from the expanding plasma stride the substrate and form a thin film with characteristic spatial thickness and composition variations.

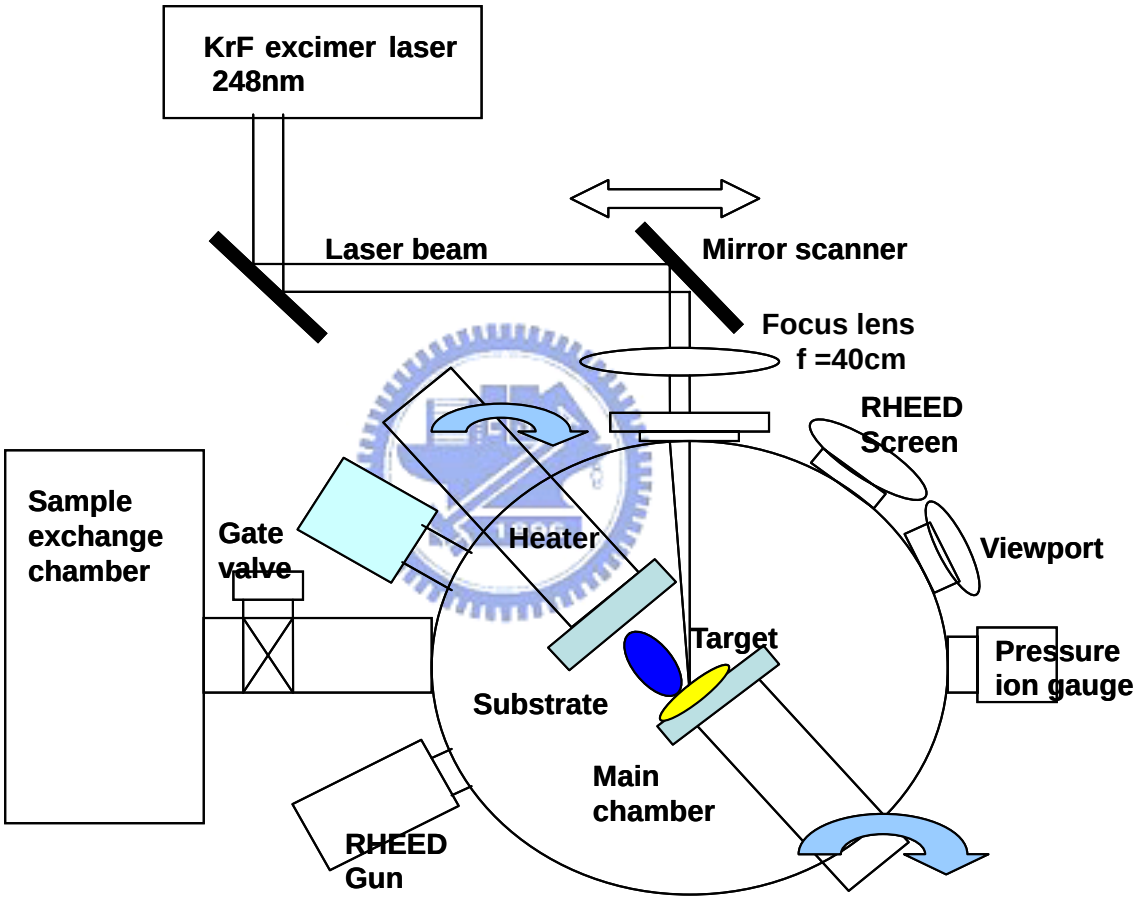

Fig. 2-2 Inner of the deposition chamber

2.3 Reflection High Energy Electron Diffraction

The reflection high-energy electron diffraction (RHEED) apparatus is one of the most useful and important surface analysis instruments in the ordinary MBE growth

chamber. It provides sensitive information of the outermost layers of atoms of the crystal before and during growth as a function of growth conditions. It is possible to obtain information concerning substrate cleanliness, smoothness, and surface structure from the RHEED patterns. In the Laser-MBE system, a collimated beam of high energy electrons in the range of 5-40 KeV is directed at a low angle of 1-2^{o} toward the sample surface orthogonal to the molecular beam paths. Because the de Broglie wavelength of electron at this energy is a fraction of atomic spacing on surface, a diffraction pattern is formed on the fluorescent screen mounted opposite to the electron source. In this configuration, the sample surface can continuously monitored without interrupting the growth procedure. Since the component of the incident electron momentum normal to the surface is very small, the penetration depth is limited to only the uppermost few atomic layers. On a smooth crystal surface with a lattice constant a_o, this acts as a two-dimensional Laue diffraction condition. Using the Ewald construction the reciprocal lattice is composed of rods in reciprocal space in the direction normal to the real surface. At high energy, the de Broglie wavelength λ of the electron is small, and the radius of the Ewald sphere $2\pi / \lambda$ is large compared to the typical reciprocal lattices, $2\pi / a_o$. In addition, the reciprocal lattice rods have finite thickness due to lattice imperfections and thermal vibrations, and the Ewald sphere also has finite thickness due to the spread in electron energy and beam divergence. As a result, the intersection of the Ewald sphere and reciprocal lattice rods occurs almost along their length, as incident in Fig. 2-3, where shows schematic diagram of the RHEED geometry with a glancing incidence beam of electrons at an incident angle θ and an azimuthal angle ϕ upon a surface plane [16]. This results in a streaked diffraction pattern normal to the shadow edge of the sample. On the contrary, in the presence of microscopic roughness on an otherwise flat surface, the diffraction pattern is formed mainly in transmission through the surface asperities

and exhibits a spotty appearance.

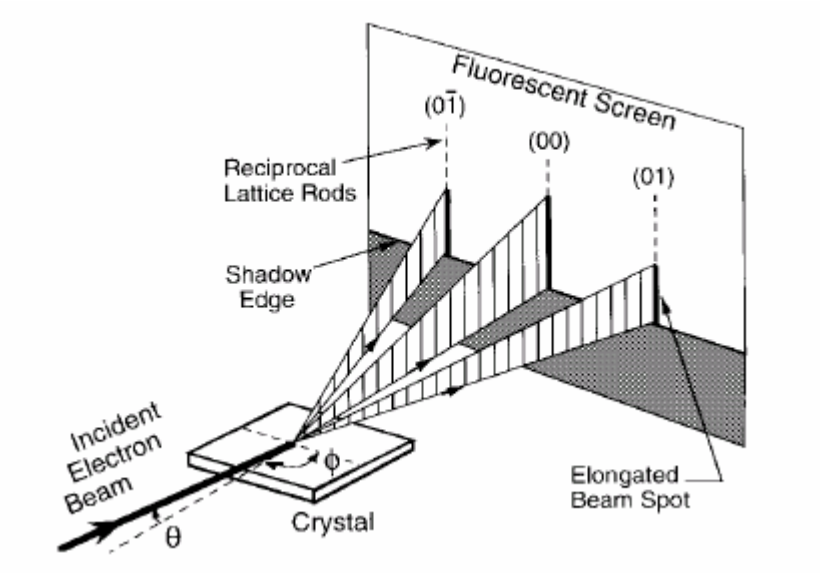

Fig. 2-3 Schematic diagram of the RHEED geometry

In kinematical scattering theory [17], the possible reflections are determined by the condition that the wave vectors k_0 and k' of the incident and diffracted beams differ by a reciprocal-lattice vector G:

$$k' - k_\circ = G \tag{2-1}$$

When considering only elastic scattering events, which means that $|k'| = |k_\circ|$, this diffraction condition can be cast into the geometrical construction of the Ewald's sphere in reciprocal space. In this construction, the tip of $k_\circ$ is attached to a reciprocal-lattice point. The sphere around the origin of $k_\circ$ with radius $k_\circ$ then defines the Ewald sphere. The magnitude of the wavevector for high-energy electrons is given by

$$k_\circ = \frac{1}{\hbar}\sqrt{2m_\circ E + \frac{E^2}{c^2}} \tag{2-2}$$

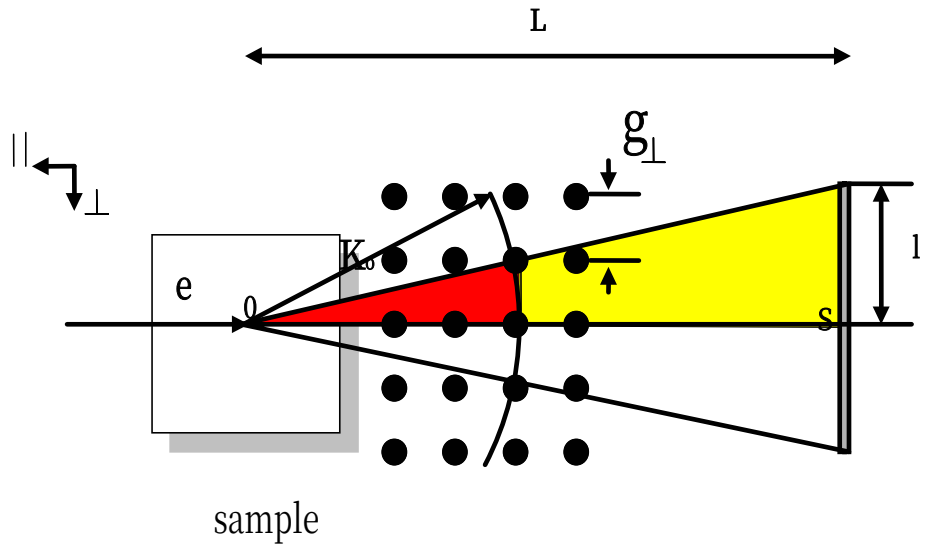

Fig. 2-4 Ewald sphere construction and diffraction geometry of RHEED

We shall show experimentally that the sampling depth of the crystal of RHEED in these cases can be very small. This implies that the periodic part of the crystal beneath the surface can usually be neglected. In the construction of the reciprocal lattice we can therefore often approximate the sampled volume by a two-dimensional layer. The reciprocal lattice then degenerates into a set of one-dimensional rods along the z direction perpendicular to the surface. Using this reciprocal lattice, we get the Ewald sphere construction used in RHEED that is shown in Fig. 2-4.

The specular reflection or specular spot S is located at the intersection of the zeroth-order Laue circle with the (00) rod, the origin of the reciprocal lattice is projected onto I, also labeled (000), where for some sample geometries the part of the incident beam that missed the sample becomes visible. Owing to the simple geometry of RHEED, the reciprocal-lattice-rod separations $g_{\perp}$ perpendicular to the beam direction can be easily determined

$$ng_{\perp} = \frac{k_{\circ}}{\sqrt{\left(\frac{nl}{L}\right)^2 + 1}} \tag{2-3}$$

which for small angled ($nl \langle\langle L$) can be approximated by

$$ng_{\perp} = \frac{nl}{L} K_{\circ} \tag{2-4}$$

Again, $n g_{\perp}$ is measured from the central rod.

2.4 X-ray diffraction

Consider hexagonal unit cell which is characterized by lattice parameters a_0 and c_0, the plane spacing equation for the hexagonal structure is

$$\frac{1}{d^2} = \frac{4}{3}\left(\frac{h^2 + hk + k^2}{a^2}\right) + \frac{l^2}{c^2} \tag{2-5}$$

Combining Bragg's law ($\lambda = 2 d \sin\theta$) with (2-5) yields :

$$\frac{1}{d^2} = \frac{4}{3}\left(\frac{h^2 + hk + k^2}{a^2}\right) + \frac{l^2}{c^2} = \left(\frac{2\sin\theta}{\lambda}\right)^2 \tag{2-6}$$

where λ is the wavelength of the x-ray source. Rearranging (2-6) gives

$$\sin^2\theta = \frac{\lambda^2}{4}\left[\frac{4}{3}\left(\frac{h^2 + hk + k^2}{a^2}\right) + \frac{l^2}{c^2}\right] \tag{2-7}$$

thus the lattice parameters can be estimated from (2-7).

2.5 Photoluminescence characterization [18]

2.5.1 Photoluminescence property

i. Free excitons:

A free hole and a free electron as a pair of opposite charges experience a coulomb attraction. Hence the electron can orbit about the hole as if this is a hydrogen-like atom. If the material is sufficiently pure, the electron and hole pair forms as exciton which then recombines and emit a narrows spectral lime. In a direct band-gap semiconductor, where momentum is conserved for radiative transition in a sample, the energy of the emitted photon is simply

$$h\nu = E_g - E_x \tag{2-8}$$

where E_x: free exciton binding energy

ii. Bound excitons:

Similar to the way that free carriers can be bound to (point-) defects, it is found that excitons can also be bound to defects shown in Fig. 2-5 [18]. A free hole can combine with a neutral donor to form a positively charged excitonic ion. In this case, the electron bound to the donor still travels in a wide orbit about the donor. The associated hole, which moves in the electrostatic field of the "fixed" dipole, determined by the instantaneous position of the electron, then also travels about this donor; for this reason, this complex is called a "bound exciton". An electron associated with a neutral acceptor is also a bound exciton. The binding energy of an exciton to a neutral donor (acceptor) is usually much smaller than the binding energy of an electron (hole) to the donor (acceptor).

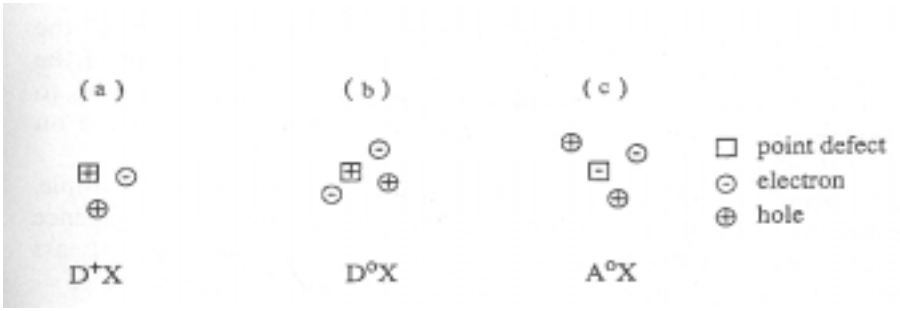

Fig. 2-5 Visualization of (a) an exciton bound to an ionized donor, (b) a neutral donor, and (c) a neutral acceptor

iii. Polaritons

A polariton is the complex resulting from the polarizing interaction between an electromagnetic wave and an oscillator resonant at the same frequency. The oscillator can be one or more atoms, electrons, or holes or their combination. Although polaritons initially have designed the interaction between excitons and photons, they can also represent the interaction between photons and optical phonons and plasmons. Phonons are collective vibrational modes of the atoms forming the crystal; plasmons are collective oscillations of the free carries.

As shown in Fig. 2-6 [18], the dispersion curve for a free exciton is a parabola, whereas that of the photon is a straight line. In the vicinity of the intersection of these two curves, the polariton-dispersion curve (dashed) exhibits a maximum interaction between the photon and the exciton. Only the lowest branch of the dispersion curve will be of interest to us. Above the knee of the polariton curve the particle will behave as a free exciton; below the knee it will behave as a photon.

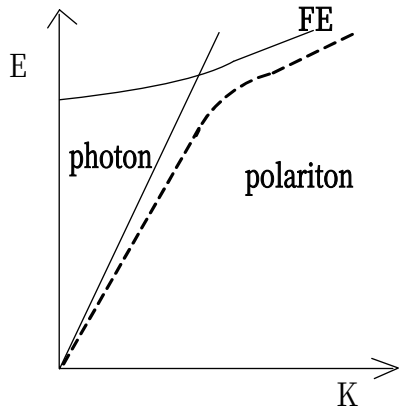

Fig. 2-6 Dispersion curves for polaritons (dotted line) and free excitons and photons (solid lines)

2.5.2 Stimulated emission and optical gain

i. Relationship between spontaneous and stimulated emission

A photon of energy hν traversing a semiconductor can stimulate a transition between two levels E_1 and E_2 whose energy difference is $E_2 - E_1 = h\nu_{12}$. (Fig. 2-7) [19] The transition can proceed either way, 1→2 or 2→1, provided there are electrons in the initial state and holes in the final state. The (1→2) transition is the absorption or pair-generation process [Fig. 2-7(a)]; if the recombination occurs in response to a passing photon, it is a "stimulated" recombination [Fig. 2-7(b)]; if it occurs without apparent provocation, it is a "spontaneous" recombination [Fig. 2-7(c)].

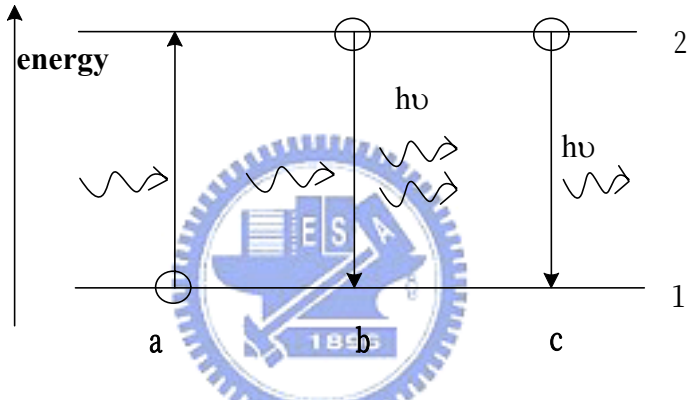

Fig. 2-7 Schematic representations of various interaction processes of light with matter namely

Chapter 3
Experimental detail

3.1 The growth of the ZnO films

3.1.1 The Laser-MBE system Layout

The system consists of two chambers, the load lock chamber (LLC) and the growth chambers (GC), as shown Fig. 3-1. There is a gate valve between the LLC and GC. A combination of scroll pump and turbo pump is used to achieve high vacuum pressure (<10^{-8} torr) in the GC. The sample is loaded from the LLC and then transfer to the GC. The GC, designed for pulsed laser ablation, is equipped with laser beam inlet and RHEED.

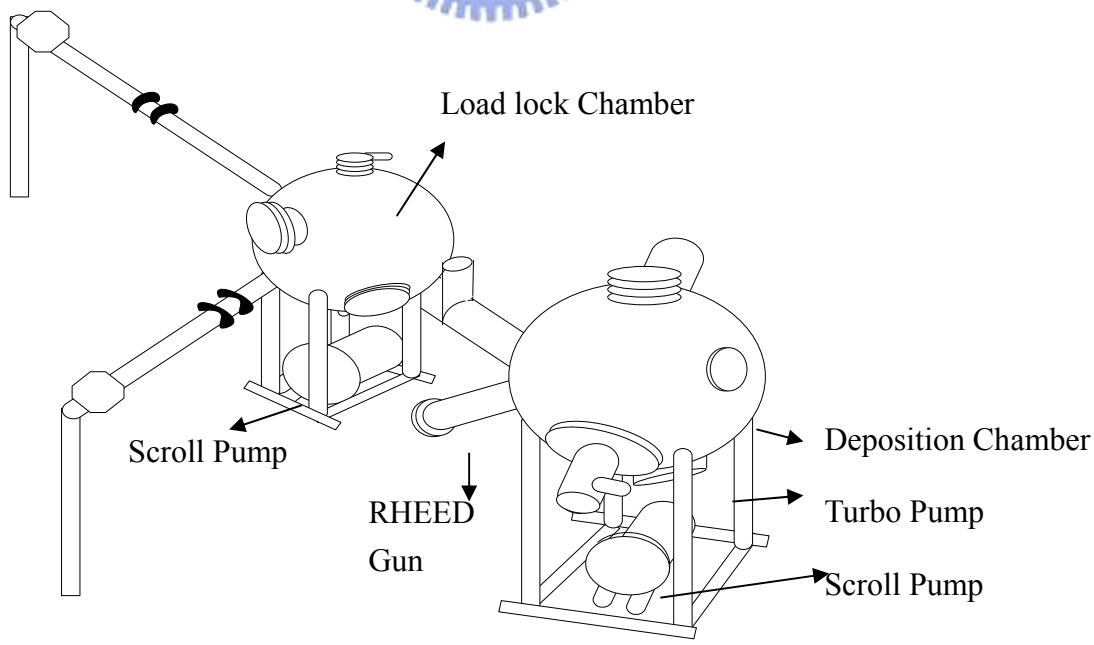

Fig. 3-1 Laser-MBE system layout

The ZnO thin films were prepared by the laser-MBE deposition utilizing a KrF pulsed excimer laser (Lamda Physics LPX 210i whose data sheet is listed in Table **3-1**).

Table 3-1 LPX210i (KrF) Specifications

Wavelength	Pulse Energy	Max. Rep. Rate	Average Power	Pulse Duration	Beam Dimension	Beam Divergence
248 nm	700 mJ	100 HZ	65 W	25 ns FWHM	5-12x23 mm^2	1 x 3 mrad

3.1.2 Target preparation

The target was prepared by commercial ZnO target with purity of 99.999% and the target size is 1" x 0.118". Before the deposition, the laser beam was ablation on the ZnO target to remove the contamination on the target surface.

3.1.3 The surface treatment of the substrate

High quality c-face sapphire wafers were used as the substrates for the growth of ZnO thin films. Before the surface treatment, the substrates were cut into a area of 20 $\times$ 10 mm^2 for the epitaxial growth. Then Al_2O_3 and SiC substrate were cleaned by using the following steps:

(1) Rinsed in D. I. water for 5 min.

(2) Rinsed in Acetone (ACE) solutions by a supersonic oscillator for 5 min.

(3) Rinsed in D.I. water for 5 min.

(4) Rinsed in Isotropic Alcohol (IPA) solutions by a supersonic oscillator for 5min.

(5) Rinsed in D.I. water for 5 min.

(6) Rinsed in H_2SO_4 : H_2O_2=3:1 for 10 min.

(7) Rinsed in D.I. water for 5 min.

(8) Dried with the gas of N_2.

After the surface treatment, the substrates were mounted on the molybdenum substrate holder and ready to grow ZnO thin films. For Si (111) substrate, it was cleaned for standard Radio Corporation of America (RCA) cleaning.

3.1.4 Operating process of the Laser-MBE system

(1) Load the substrate holder (with the substrate) into the load lock chamber and turn on the scroll pump.

(2) After the pressure of the chamber was pump down to lower than $3x10^{-2}$ torr, the turbo-pump was turned up.

(3) The pressure of the chamber could reach 10^{-8} torr in two hours. Only at this condition, we can open the gate valve between the load lock and main chamber. We use the magnetically coupled transfer arm to transfer the substrate holder from the load lock chamber into the main chamber.

(4) After transferring substrate, close the gate valve.

(5) Adjust the distance between the substrate and ZnO target to reach the appropriate position.

(6) Make sure that the water cooling system was working.

(7) Turn on the thermal controller and power supply. Set the needed thermal program.

(8) Ensure the substrate temperature is reached. Wait for a few minutes to let the chamber pressure decline to $7x10^{-9}$ torr.

(9) Turn on step motor to start the mirror scanner. Turn on target manipulator and sample manipulator rotation to make the thin film uniform.

(10) Turn on the laser and start to grow thin film.

(11) After thin film growth was completed, open the gate valve and use the magnetically coupled transfer arm to transfer the sample from the main chamber to the load lock chamber.

(12) Stop the turbo pump and the scroll pump. When the blades of the turbo pump stop, we can vent the load lock chamber by insert N_2 gas.

After the surface treatment, substrate was loaded in the chamber with the base pressure of 1×10^{-9} torr [see Fig. 2-2] and we used a focus lens (f= 40 cm) to converge the laser beam through a window of chamber onto the target, which makes 45 degree to the normal of the target. Within the chamber, a ZnO ceramic target (99.999%) was located in front of the substrate holder at a distance of 5 cm and was ablated by a KrF excimer pulsed laser with the wavelength, pulse duration, repetition rate, and laser fluence of 248 nm, 25 ns, 5 Hz, respectively. At the same time, the laser beam was scanning by moving reflection mirror, which is carried by step motor to prevent laser hitting at the same point on the target that leads to non-uniform film growth. In order to grow a uniform thin film, the target holder and sample holder rolled during thin film deposition.

3.2 Determination of structures and synthesis of the ZnO

thin films

3.2.1 X-ray diffraction

The crystal structures of the as-grown as well as post-annealed thin films were inspected by a Bede D1 diffractometer at Industrial Technology Research Institute using a CuK X-ray source (λ=1.5405 $\mathring{A}$). The scanning step is 0.02^{o} and scanning rate is 4 degree/min. Fig. 3-2 shows XRD ω–2θ scans geometry of ZnO (0 0 2) and (1 1 0) diffraction peaks. The dashed lines mean the trajectory of the incident beam and the detector to be in motion.

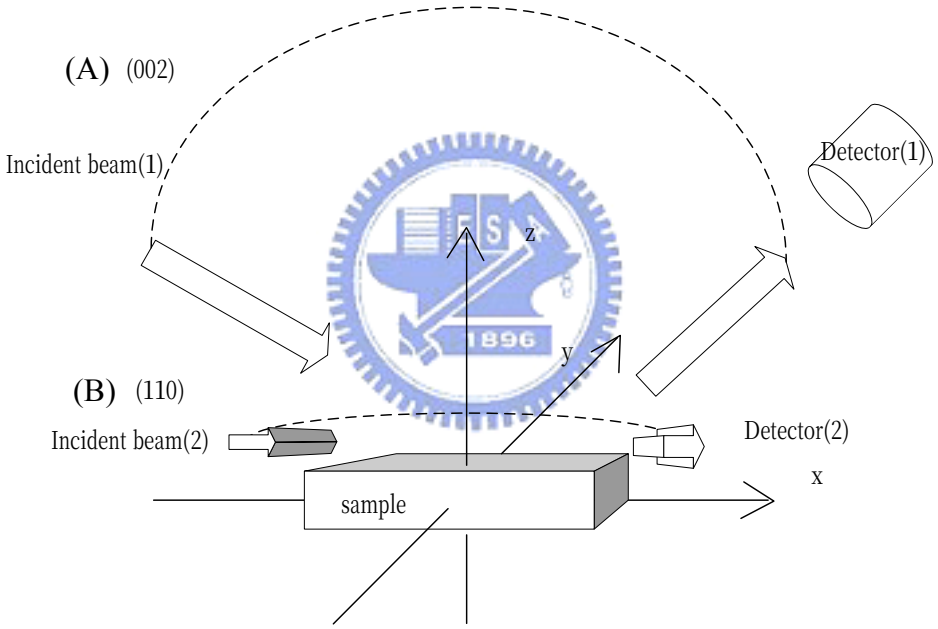

Fig. 3-2 XRD ω–2θ scans geometry of ZnO (A) (002) and (B)(1 1 0) diffraction peaks.

3.3 Measurements of optical properties

3.3.1 Photoluminescence detection system

A He-Cd laser (Kimmon IK5552R-F) operating at the 325 nm UV line is

commonly utilized as pumping source for PL. As shown in Fig. 3-3, the block diagram of PL detection system includes mirror, focusing and collecting lens, the sample holder and the cooling system. We utilized two single-grating monochromators (TRIAX 320), one equipped with a CCD detector (CCD-3000), and the other equipped with a photo-multiplier tube (PMT-HVPS), which is equipped with a photon counter for detection. The normal applied voltage of PMT is 0.8 KV. Moreover, we used a standard of fluorescent lamps to calibrate our spectral response of spectrometer and detector. The PL signals are exposed about 0.1 sec at the step of 0.1 nm. The data are transmitted through a GPIB card and recorded by a computer. TRAIX 320 has a focal length of 32 cm with an optional side exit slit and has three selective 600, 1200 and 1800 grooves/mm gratings. When the entrance and exit slits are both opened to about 50 μm, the resolution is about 0.1 nm for the monochromator with PMT. The low-temperature PL measurements were carried out using a closed cycle cryogenic system.

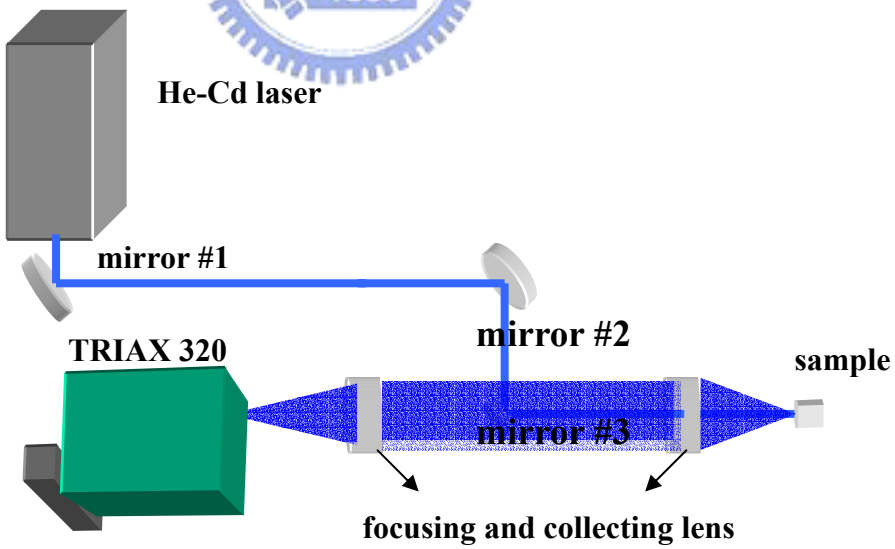

Fig. 3-3 PL detection system

3.3.2 Stimulated emission and optical gain detection system

For high power excitation measurements, we used a third harmonic of Nd:YVO_4 laser (3.51 eV photon energy) with a pulse width of ~500 ps and a repetition rate of 1kHZ.. As shown in Fig. 3-4, the beam size of Nd:YVO_4 laser was expanded to two times larger than the original. Then it was focused on the sample surface using a cylindrical lens to form a rectangular stripe of L×H, 300×145.08 μm^2, where L denotes the total length of excitation stripe, which can be tuned by a slit and a movable knife. The distance from the sample edge to the excited region remains unchanged when the length of the excitation stripe is varied. Emission from the sample edge was collected onto a fiber connected to and recorded by the monochromator, which is equipped with a CCD detector.

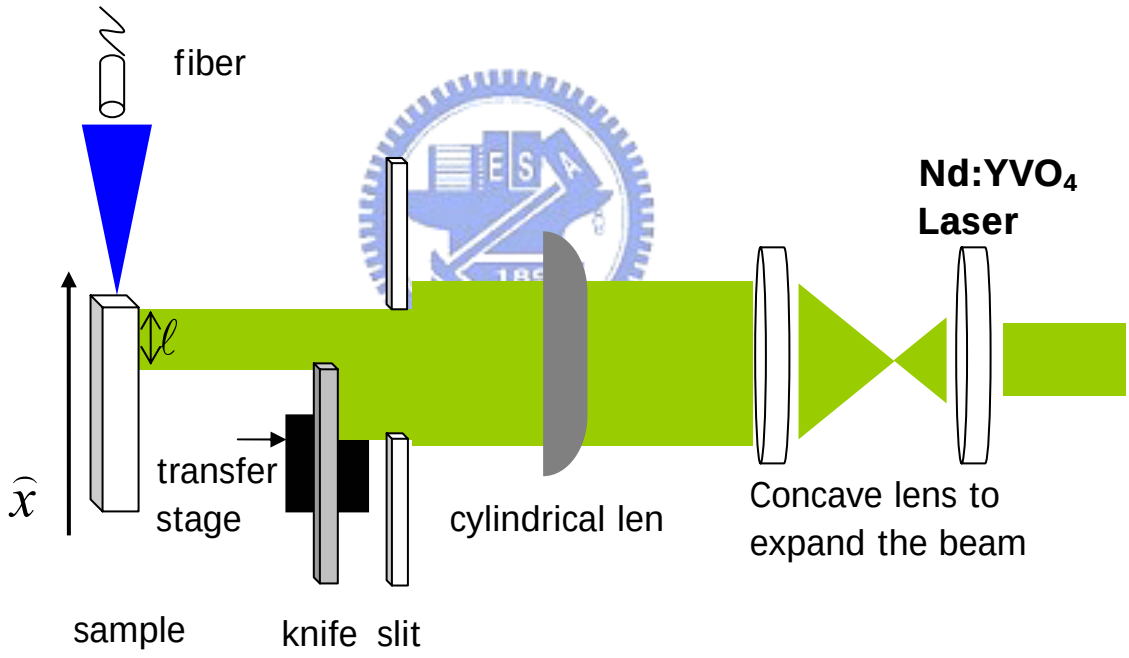

Fig. 3-4 Stimulated emission and optical gain detection system

3.3.3 Optical gain measurement

To measure the optical gain we excite the sample with a stripe and vary the stripe of light beam length. If there is only spontaneous emission we expect in the

transparent spectral region a linear increase of the luminescence with increasing stripe length. For stimulated emission we expect an exponential increase of the PL. The photoluminescence emitted to the x direction [see Fig. 3-4] (in-plane) is given by (3-1). The change of the PL intensity in x direction is given by the spontaneous emission to the x direction $A \times I_{spont}$ (hν) and the stimulated emission g'(hν)×I (x, hν)

$$\frac{\partial}{\partial x} I(x,h\upsilon) = A \times I_{spont}(h\upsilon) + g'(h\upsilon) \times I(x,h\upsilon) \tag{3-1}$$

where I_{spont} (x, hν) is spontaneous emission to the x-direction, A is area of the stripe, g'(hν) is net optical gain, g' = g-α where g is gain coefficient, and α is absorption coefficient, respectively. By integrating e.g.(3-1), one obtains (3-2) the dependence of the PL intensity depending on the stripe length ℓ and the optical gain g is

$$I(\ell, h\nu) = \frac{I_{spont}(h\nu) \times A}{g'(h\nu)} \left(e^{g'(h\nu) \times \ell} - 1 \right) \tag{3-2}$$

Chapter 4
Results and Discussion

This chapter is classified into three parts to discuss the structure and optical properties of the ZnO thin films. In the first part of this chapter, the crystalline and structure properties of ZnO thin films grown on various substrates will be discussed. The i*n-situ* monitoring RHEED and ω–rocking curve can determinate the crystalline quality of the ZnO thin films on different substrates. Second, we will focus on the influence of the biaxial strain on the energy of exciton at RT. The *ex-situ* XRD measurement can determine the in-plane lattice constants. In the last part, we are interested in the optical gain of ZnO epilayer with good crystalline quality. The net gain was obtained from the PL spectra at different pumping intensities. The mechanism of the optical amplification will be reported.

4.1 Crystalline quality of the ZnO thin films on different substrates

In this section, the residual stress of the ZnO thin films grown on *c*-plane Al_2O_3, Si (111) and SiC (001) was investigated. The ZnO/Al_2O_3, ZnO/Si (111) and ZnO/SiC samples were all grown under similar condition at 600^{o}C for 2 hours by the Laser-MBE system and *in-situ* annealing for 1 hour at 700^{o}C. The thickness of the ZnO/Al_2O_3 sample is 1.56 μm and those of the ZnO/Si (111) and the ZnO/SiC samples are 0.6 μm. All samples are unintentionally doped.

4.1.1 RHEED observation

Fig. 4-1 shows the Al_2O_3 substrate after the thermal treatments along [1-100] and [1-210] azimuths [Fig. 4-1(a)] and the ZnO epilayers after the deposition of about 2 nm along [2-1-10] and [1-100] azimuths [Fig. 4-1(b)]. The growth temperature for this sample is 600°C. Before the deposition, the RHEED pattern of the Al_2O_3 substrate shows sharp streaky, which indicates a clean and flat surface. At the initial stage of ZnO deposition, the RHEED pattern of the Al_2O_3 substrate disappears and a diffuse streaky pattern evolves.

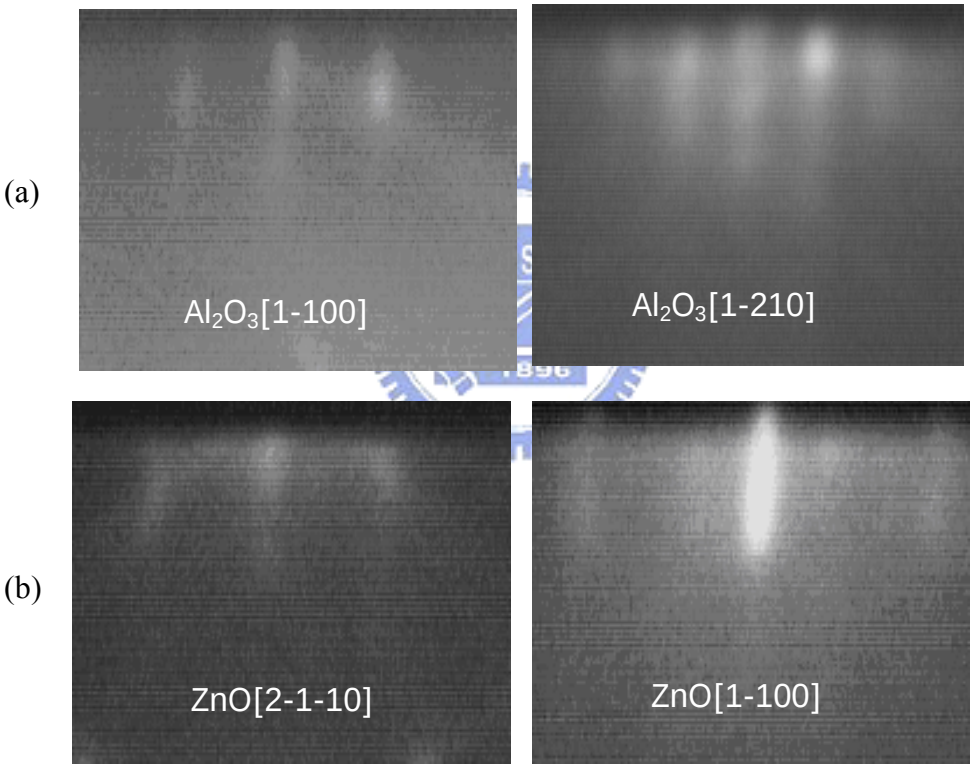

Fig. 4-1 RHEED patterns of (a) the Al_2O_3 substrate and (b) the ZnO epilayers along [2-1-10] and [1-100] azimuths

According to the previous pioneer's report [20], the ZnO epilayer and the Al_2O_3 substrate have their *c*-axis aligned parallel. The [2 -1 -1 0] direction of ZnO aligns with the [1 -1 0 0] direction of Al_2O_3, and the [1 -1 0 0] direction of ZnO aligns with the [1 -2 1 0] direction of Al_2O_3 [Fig. 4-2] [20]. The 30° rotation of the crystal

orientation of the ZnO epilayer against the Al_2O_3 substrate occurs because the ZnO lattice aligns itself with the oxygen sublattice of Al_2O_3; with this, the lattice mismatch is reduced from around 32% to 18% [1].

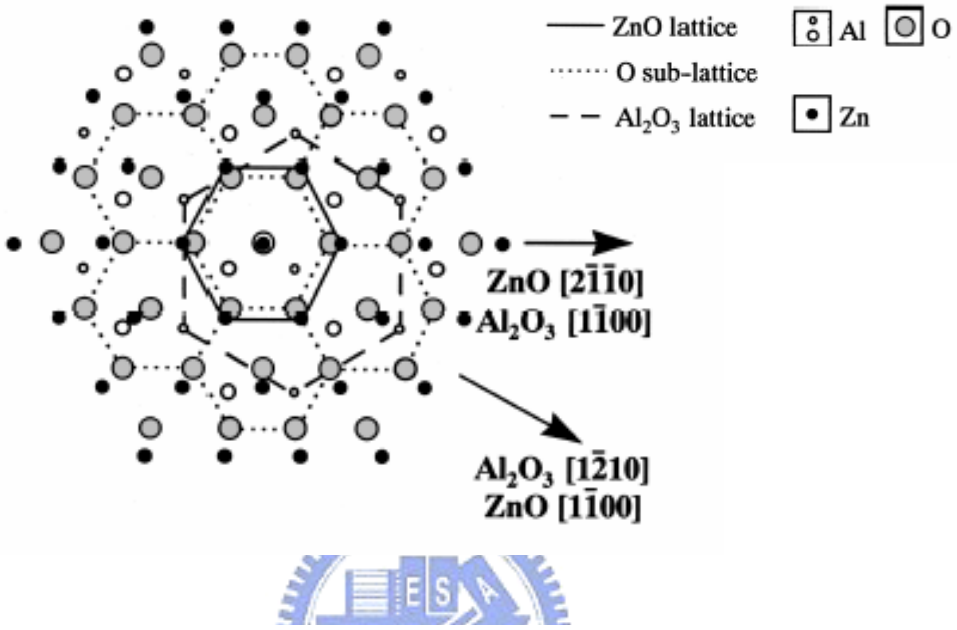

Fig. 4-2 Schematic diagram shows the epitaxial relationship of ZnO (0001) grown on *c*-plane Al_2O_3. [23]

Fig. 4-3 shows the RHEED pattern of *c*-plane Al_2O_3 along the [1-100] azimuths, Si(111) and SiC substrate after thermal treatment as well as ZnO thin films along the [1-100] azimuths on the above mentioned substrates. RHEED patterns of the ZnO thin films grown on the Al_2O_3 substrate show streaky [see Fig. 4-3(b)], besides those are spotty on Si (111) and SiC substrates [Fig. 4-3(d) and Fig. 4-3(f)]. In the previous study [1], the RHEED patterns change from streaky to spotty during the growth of the films on the substrate. It indicates a roughening of the growth surface. The morphology evolution is related to a transition of the epitaxial growth mode from two-dimensional (2D) nucleation to three-dimensional (3D) one. Therefore, it can be deduced that the morphology of the ZnO thin films on *c*-plane Al_2O_3 is smoother than those on Si (111) and SiC.

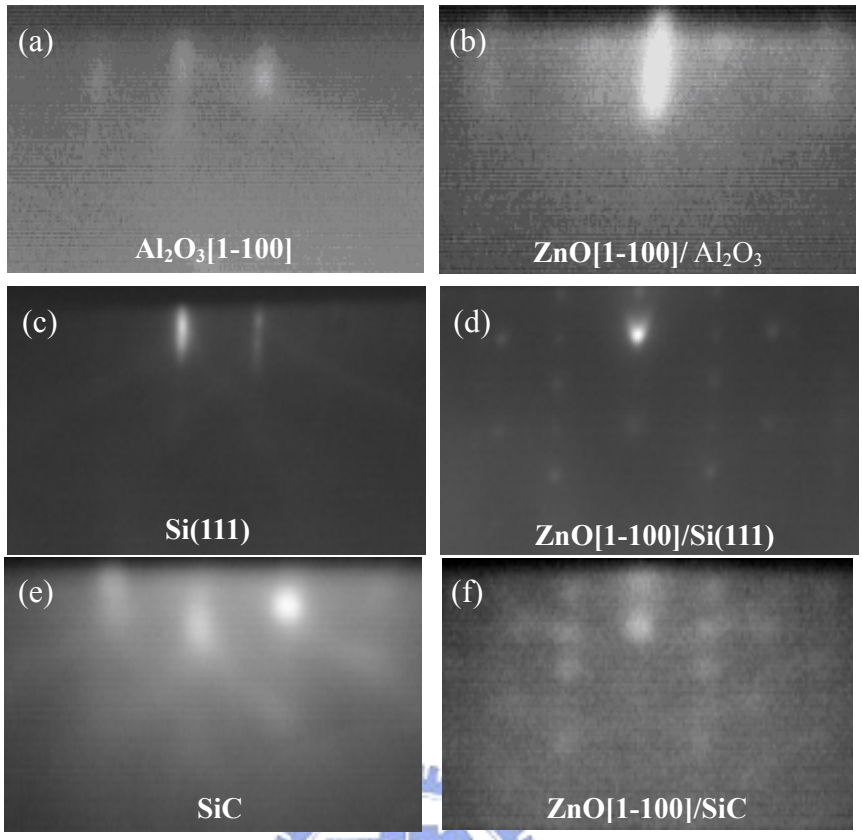

Fig. 4-3 RHEED patterns of (a) *c*-plane Al_2O_3[1-100], (c) Si(111) and (e) SiC substrate and ZnO thin films on above mentioned substrates.

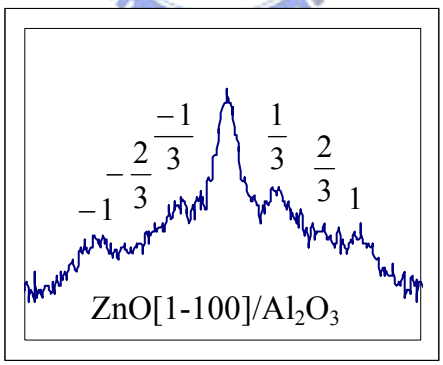

Fig. 4-4 Intensity profiles of RHEED patterns of ZnO thin films on *c*-plane Al_2O_3 along [1-100] azimuth.

Fig. 4-4 shows the line profile of the RHEED intensity of the ZnO/Al_2O_3 sample along [1-100] azimuth and displays the (3x3) reconstructed of ZnO thin films [21]. Surface reconstruction can be a consequence of a rearrangement of broken covalent or

ionic bonds at the surface. Under such conditions the atoms at the surface bunch into rows with alternately larger and smaller spacing than those in the bulk. That is, for some crystals held together by valence bonds, creation of a surface would leave unsaturated bonds dangling into space. The energy may then be lowered if neighboring atoms approach each other and form bonds with their otherwise unused valence electrons [22]. Previous studies [23],[24],[25] concluded that both the Zn-terminated ZnO (0001) and O-terminated ZnO (000-1) surface have (1x1) surface structure which deviates little from the bulk truncated surface [24]. However, from the theoretical viewpoint, for the polar surface such as ZnO (0001) and ZnO (000-1), the presence of a surface dipole perpendicular to the ideal bulk truncated surface suggests that these surfaces will be unstable. This has lead to the hypothesis of ZnO surface reconstruction [26]. The surface reconstruction reflects the surface stoichiometry, which depends much on the ambient surrounding of the surface. Our Laser-MBE growth environment is very different from those in the previous surface analytic experiments [23],[24],[25].

4.1.2 XRD ω–rocking curve

Fig. 4-5 shows the XRD ω–rocking curves of the ZnO (002) diffraction peak on Al_2O_3, Si (111) and SiC samples, respectively. The FWHM of the (002) ω–rocking curves for these three samples are 207 arcsec, 2624 arcsec and 3082 arcsec, respectively. Compared with the FWHM of (002) ω–rocking curve for the ZnO/Si (111) and ZnO/SiC samples, the ZnO/Al_2O_3 sample gives a narrower width, which implies the less tilt in the *c* planes. These properties of the (002) diffraction peak indicate the perfect ordering along the growth direction of ZnO (001) as a consequence of well controlled layer-by-layer epitaxy. The FWHM of ZnO/Si (111) and ZnO/SiC samples are larger than the previous reports [27],[28]. Thus the quality

of the ZnO/Si (111) and ZnO/SiC is not good.

4.1.3 Phi Scan

Upper part of Fig. 4-6 (a), (b) and (c) show phi scan of each (202) peak for ZnO on Al_2O_3, Si and SiC. Lower part of Fig. 4-6(a), (b) and (c) show ϕ scan of each (202) peak for the substrates. Fig. 4-6(a) shows six-fold symmetry of ZnO thin films and Al_2O_3. ϕ scan of each ZnO (202) peaks were separated by 60^o and the Al_2O_3 (202) peaks shift 30^o compared to those of the ZnO thin films. This indicates a 30^o rotation of the ZnO unit cell with respect to that of Al_2O_3. Combining the results of RHEED observation and XRD ϕ scan, the epitaxial relationship between ZnO and Al_2O_3 is $[2\text{-}1\text{-}10]_{ZnO} \| [1\text{-}100]_{Al_2O_3}$. Fig. 4-6 (b) shows three-fold symmetry of Si (111) substrate, but there is no peak in the ϕ scan of the ZnO (202) thin films. It indicates poor quality of the ZnO thin films onto Si (111). Fig. 4-6 (c) shows ϕ scan of each (202) peak for ZnO on SiC. The ZnO (202) peaks were separated by 60^o and the SiC (202) peaks appeared at the same angles as those of ZnO. This suggests that ZnO was also epitaxially grown on SiC and the same stacking orientation as the Wurtzite SiC.

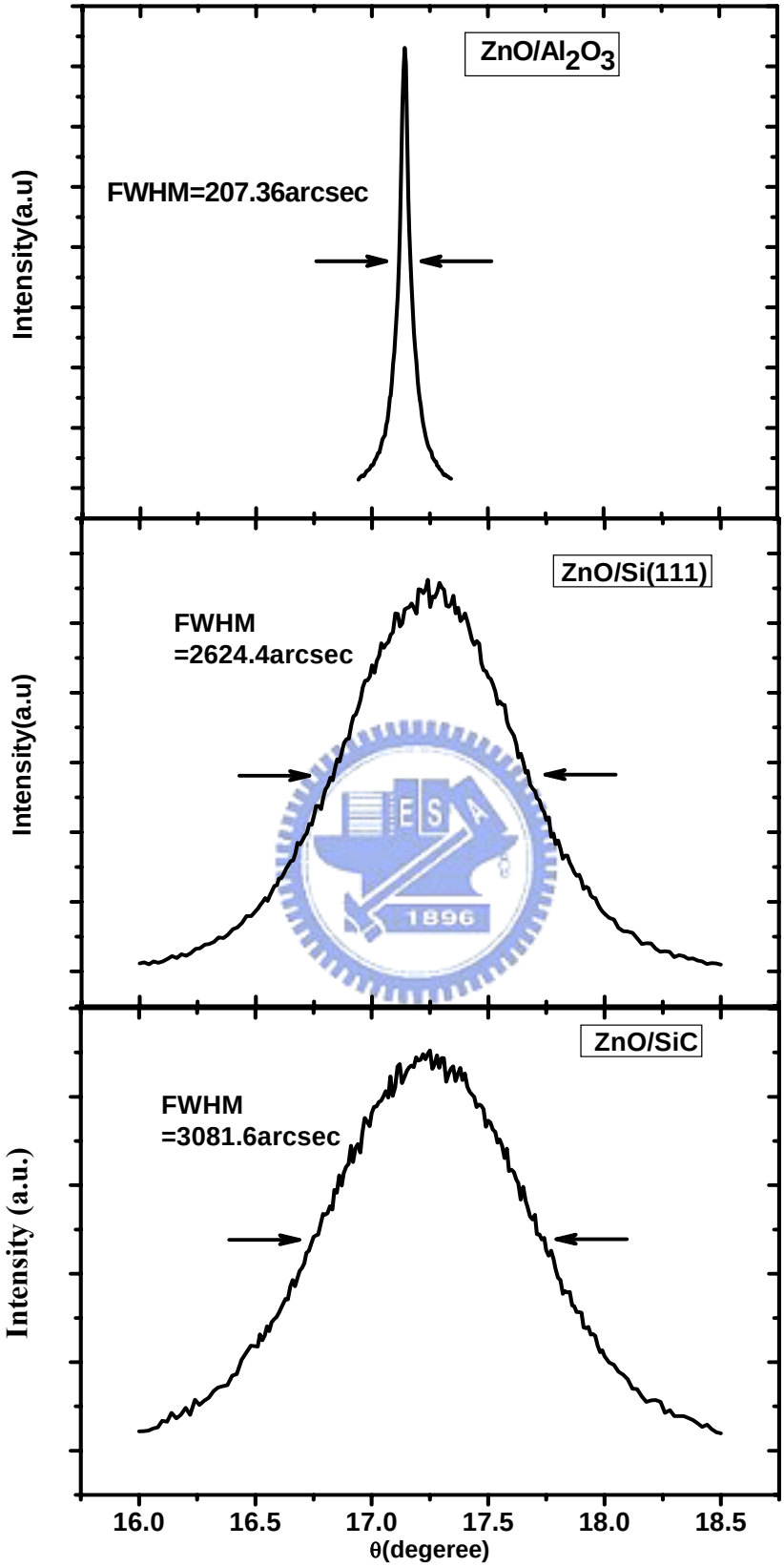

Fig. 4-5 A set of ω–rocking curve of the ZnO (002) peak on (a) Al_2O_3 (b) Si (111) (c) SiC substrates

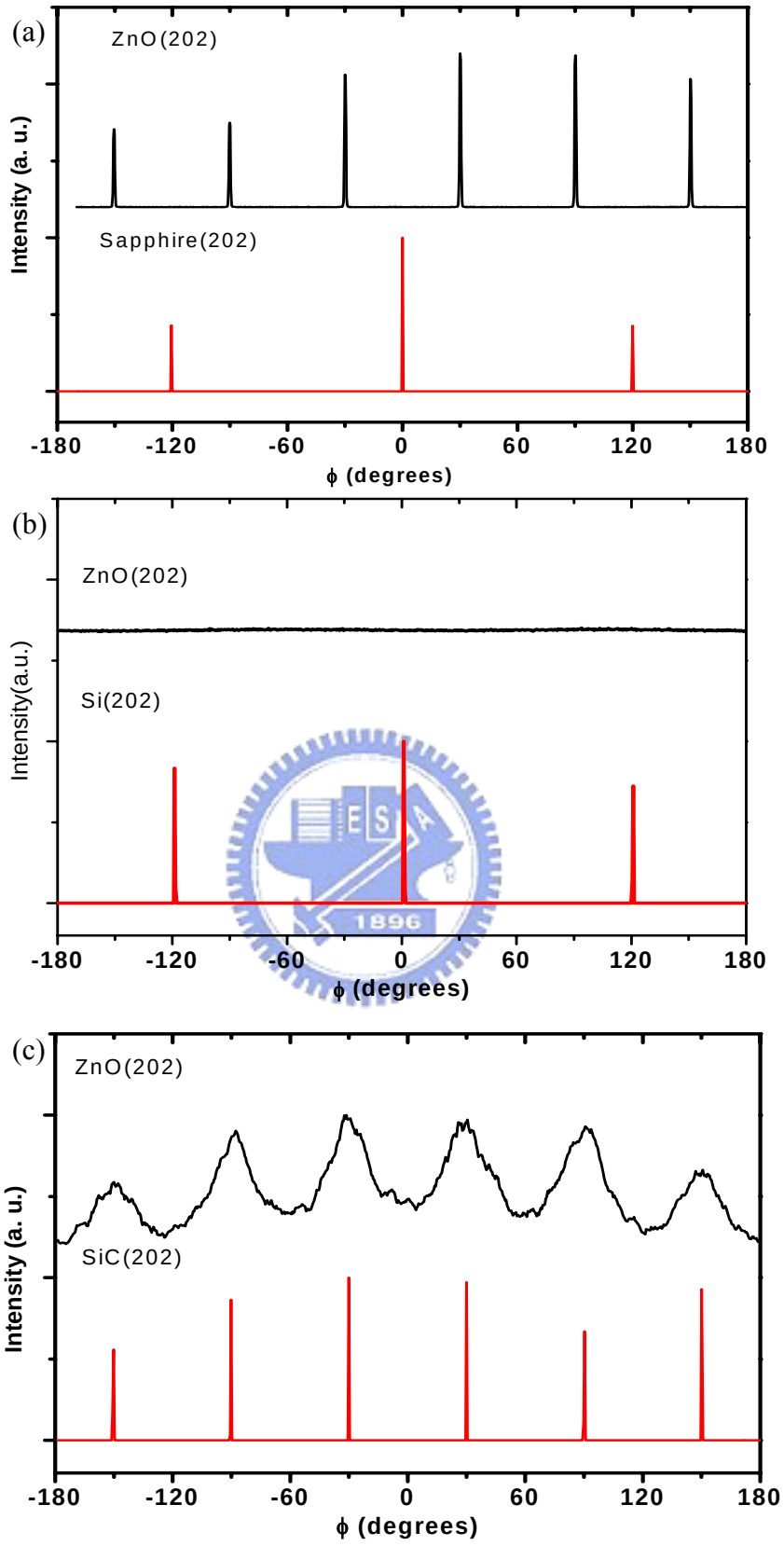

Fig. 4-6 A set of in-plane ϕ scan of the ZnO thin films (202) and the substrates (202) peak (a) Al_2O_3; ZnO/Al_2O_3 (b) Si (111); ZnO/Si(111) (c) SiC; ZnO/SiC.

4.2 Effect of Biaxial Strain on ZnO Thin Films

In this section, we use the *ex-situ* XRD ω-2θ scan on (002) and (110) reflections to determine the in-plane and out of the plane lattice constants of the three samples above mentioned. Compared to the in-plane lattice constant of the ZnO bulk, biaxial strain is observed between the ZnO epilayer and the substrates. The biaxial strain also induces the variation of the free exciton emission energy of the ZnO thin films on different substrates.

4.2.1 Lattice determination by XRD ω-2θ scan

The *c*- and *a*-axis lattice parameters of the ZnO thin films on different substrates were obtained using the XRD ω-2θ scan on the (002) and (110) reflections. The *c*- and *a*-axis can be calculated by (4-1) which has been derived in Chapter 2.

$$\sin^2\theta = \frac{\lambda^2}{4}\left\{\frac{4}{3}\left(\frac{h^2+hk+k^2}{a^2}\right)+\frac{l^2}{c^2}\right\} \tag{4-1}$$

Fig. 4-7 shows the (002) peak of the ZnO/Al_2O_3, ZnO/Si (111), ZnO/SiC samples at $2\theta = 34.347^o$, 34.570^o and 34.51^o, which determinate out of plane lattice constant *c* equal to 5.2172 Å, 5.1894 Å and 5.1936 Å, respectively. Fig. 4-8 shows the (110) peak of the ZnO/Al_2O_3, ZnO/Si (111), ZnO/SiC samples at $2\theta = 56.739^o$, 56.517^o and 56.46^o, which determinate in-plane lattice constant *a* equal to 3.2424 Å, 3.256 Å and 3.253 Å, respectively. Notice that lattice constants of the bulk ZnO are *a* = 3.249 Å and *c* = 5.207 Å. Although the strain between the film and the substrate induces the variation of the in-plane and out of plane lattice constants, the volume of a unit cell have to be fixed.

Referring to the material parameters [12],[29], it is not difficult to understand

why the opposite stress states exist in ZnO epilayers grown on Si versus on sapphire. For ZnO/Si system, the lattice constant of ZnO is smaller than that of Si [the atomic spacing in the (111) plane of Si is 3.84 Å] and its thermal expansion coefficient is larger than that of Si. Both lattice and thermal mismatches lead to the tensile stress in the ZnO epilayer. For the case of ZnO/Al_2O_3, it is known that the lattice of epitaxial ZnO rotates by 30^o with respect to that of Al_2O_3, and so the atomic spacing of the substrate parallel to a-axis of ZnO is only 2.75 Å. Consequently, epitaxial ZnO layer is expectedly compressively stressed. For sample ZnO on SiC, however, the lattice constant and the thermal expansion coefficient of ZnO is larger than those of Si. Both lattice and thermal mismatches between the epilayer and the substrate are relatively small, where the lattice constant of ZnO is slightly larger than that of SiC. It is thus somewhat surprising to observe the relative larger stress present in ZnO and the strain is tensile. We attribute such a result to the effect of thermal expansion. Stress is built in film during sample cooling from deposition temperature to RT after growing and this stress can overcompensate that due to lattice constant mismatch in this case.

Fig. 4-9 shows the lattice constant *a* vs. *c* for ZnO thin films grown on Al_2O_3, Si (111) and SiC substrates. For comparison, the lattice constants of ZnO bulk reported by R. Paszkiewicz et. al. [14] are plotted together in Fig. 4-9. It exhibits the linear relationships between the lattice constants and the epitaxial layers deformed elastically by stress in the epilayers.

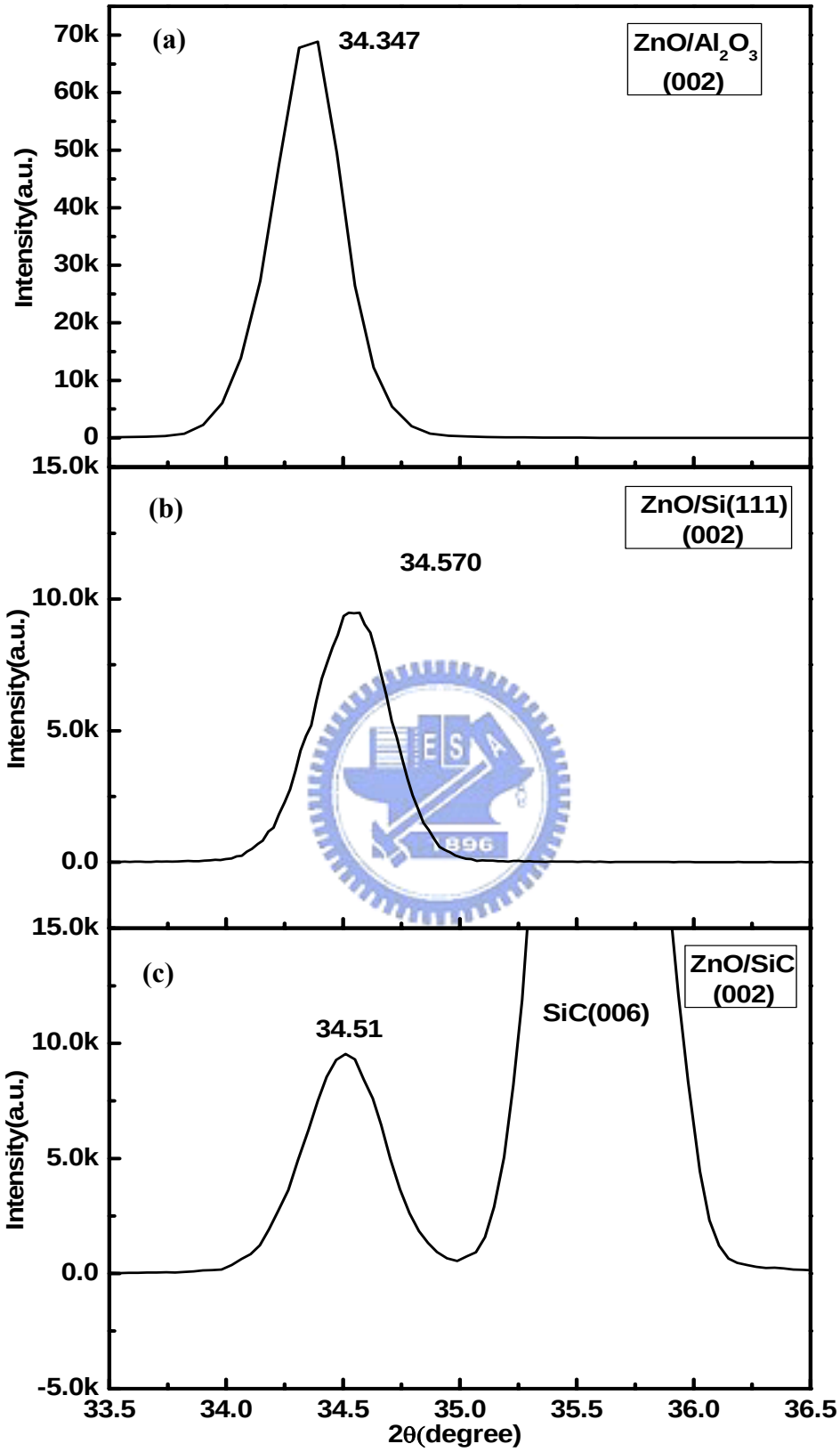

Fig. 4-7 XRD ω–2θ scan (002) of the ZnO/Al_2O_3, ZnO/Si (111) and ZnO/SiC samples

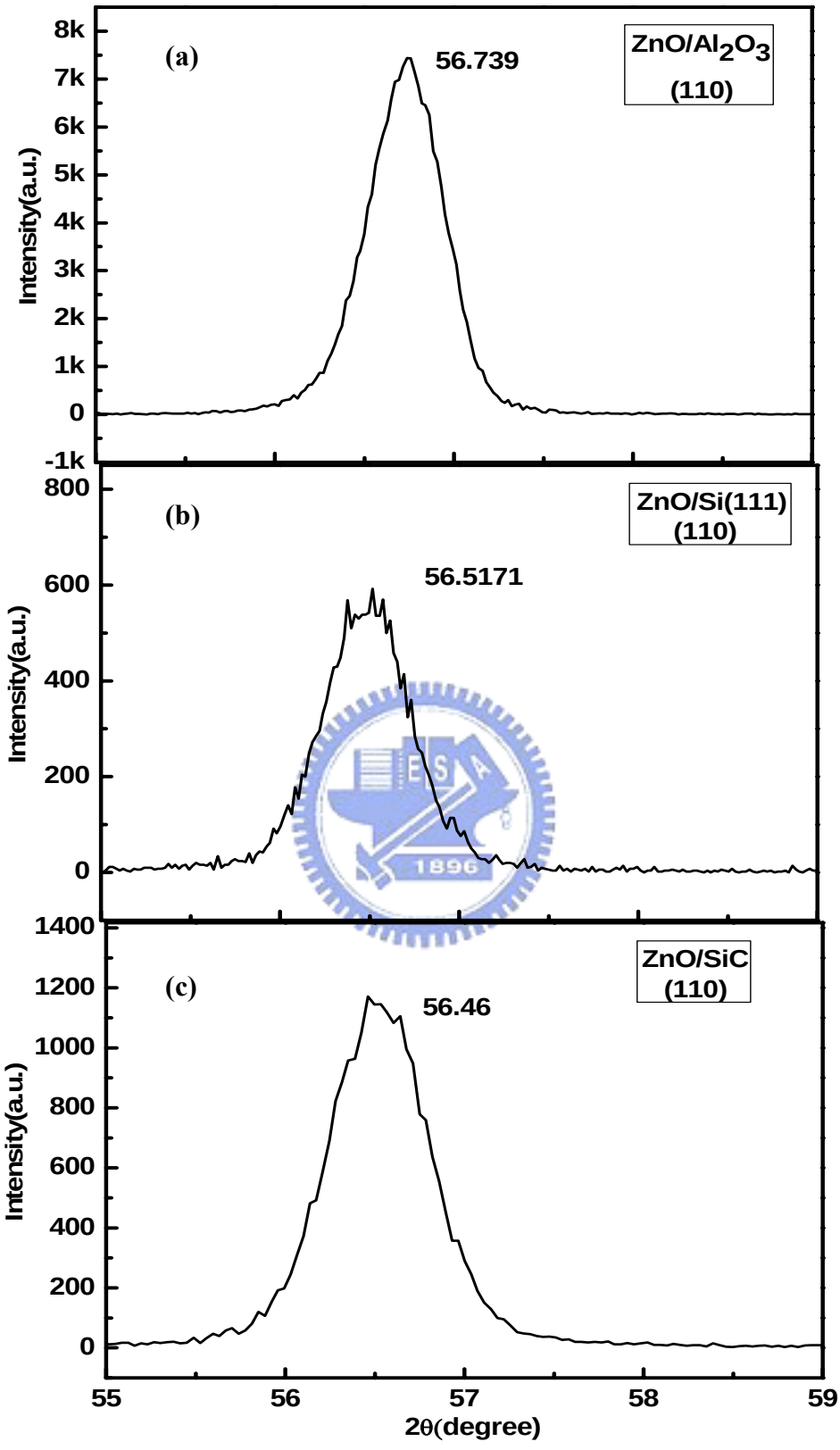

Fig. 4-8 XRD ω–2θ scan (110) peak of the ZnO/ Al_2O_3, ZnO/Si (111) and ZnO/SiC samples

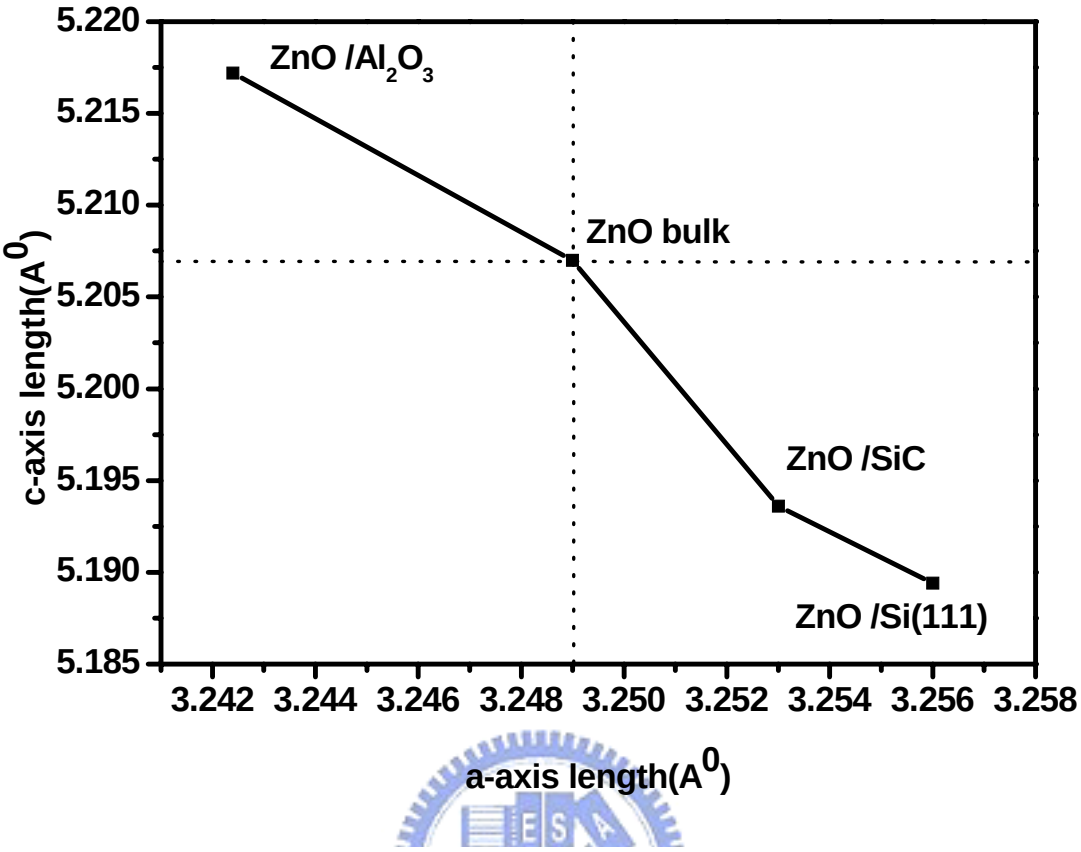

Fig. 4-9 Length of the *a*-axis is plotted against the length of the *c*-axis for the ZnO thin films grown on Al_2O_3, Si (111) and SiC.

4.2.2 Photoluminescence spectra

In order to identify the origin of the RT emission, we measured the temperature dependent photoluminescence. Fig. 4-10 shows the emission spectra of the ZnO thin films on Al_2O_3 measured at in the temperature ranging from 10 K to 300 K. At low temperature, the spectra are dominated by the neutral-donor bound exciton (D^oX) emission at 3.366 eV, which is consistent with previous report [30]. On the lower energy region of the D^oX peak, the emissions of the 1 LO-phonon replicas and 2 LO-phonon replicas are observed. With increasing temperature, the D^oX emission rapidly decreases, and is hardly resolved above 100 K. At the onset of bound exciton decay, a feature at 3.380 eV becomes stronger and finally dominates the spectrum even up to RT. The feature is assigned to free exciton emission due to its

narrow line width and its temperature dependence of emission intensity. The peak of the free exciton emission energy at RT is 3.293 eV. This result is in agreement with the literature result [30].

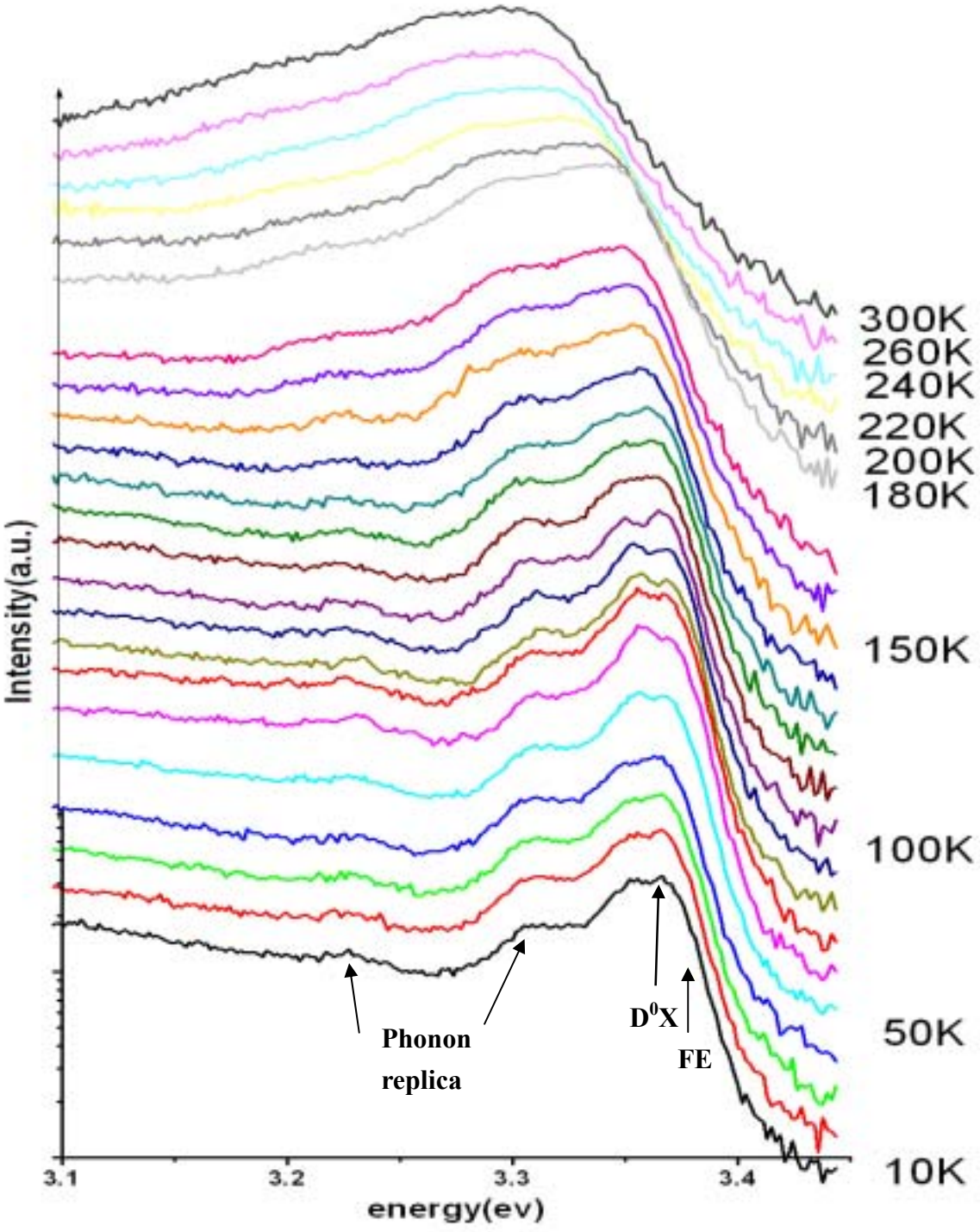

Fig. 4-10 Emission spectra of the ZnO thin films on Al_2O_3 in the temperature range 10-300K.

Fig. 4-11 shows a set of PL at RT for the ZnO/ Al_2O_3, ZnO/Si (111) and ZnO/SiC samples used for Fig. 4-3 (b), (d) and (f). As grown on different substrates, the optical properties of the ZnO thin films are also different. The full width at half maximum (FWHM) of the free exciton emission for the ZnO/Al_2O_3 [100 m eV] and ZnO/Si (111) [100 m eV] samples was narrower than that for the ZnO/SiC [146.98 m eV] sample. Besides, the intensity of the deep level emission of three samples is the lowest for the ZnO/Al_2O_3 sample, then the ZnO/Si (111) sample and the ZnO/SiC sample sequence. Usually, the quality of the optical property depends on the structure. The deep-level emission is usually related to structural defects and impurities. However, the structural defects depend on growth conditions as well as the lattice mismatch. Another feature of the PL spectra is the long tail extending from the near band edge emission, which is usually caused by band structure deformation resulting from lattice deformation. As discussed previously, the large lattice mismatches result in an interfacial region in the ZnO epilayer with a higher density of defects. This region may be responsible for the long band edge tail in the PL spectra [30].

A tensile stress will result in a decrease of energy band gap while a compressive strain causes increase of the band gap [12]. Fig. 4-12 depicts exciton energies of ZnO layers as a function of strain along the *a* axis. The strain has been calculated using the $\varepsilon_{xx} = (a-a_O)/a_O$ relation, where *a* is the measured lattice constant from XRD (110) reflection and a_O is the unstrained lattice constant. The FE emission of the ZnO bulk constant was cited from Ref [30]. An approximate tendency was in agreement with a tensile stress induces free exciton emission energy blue shift and a compressive stress induces red shift.

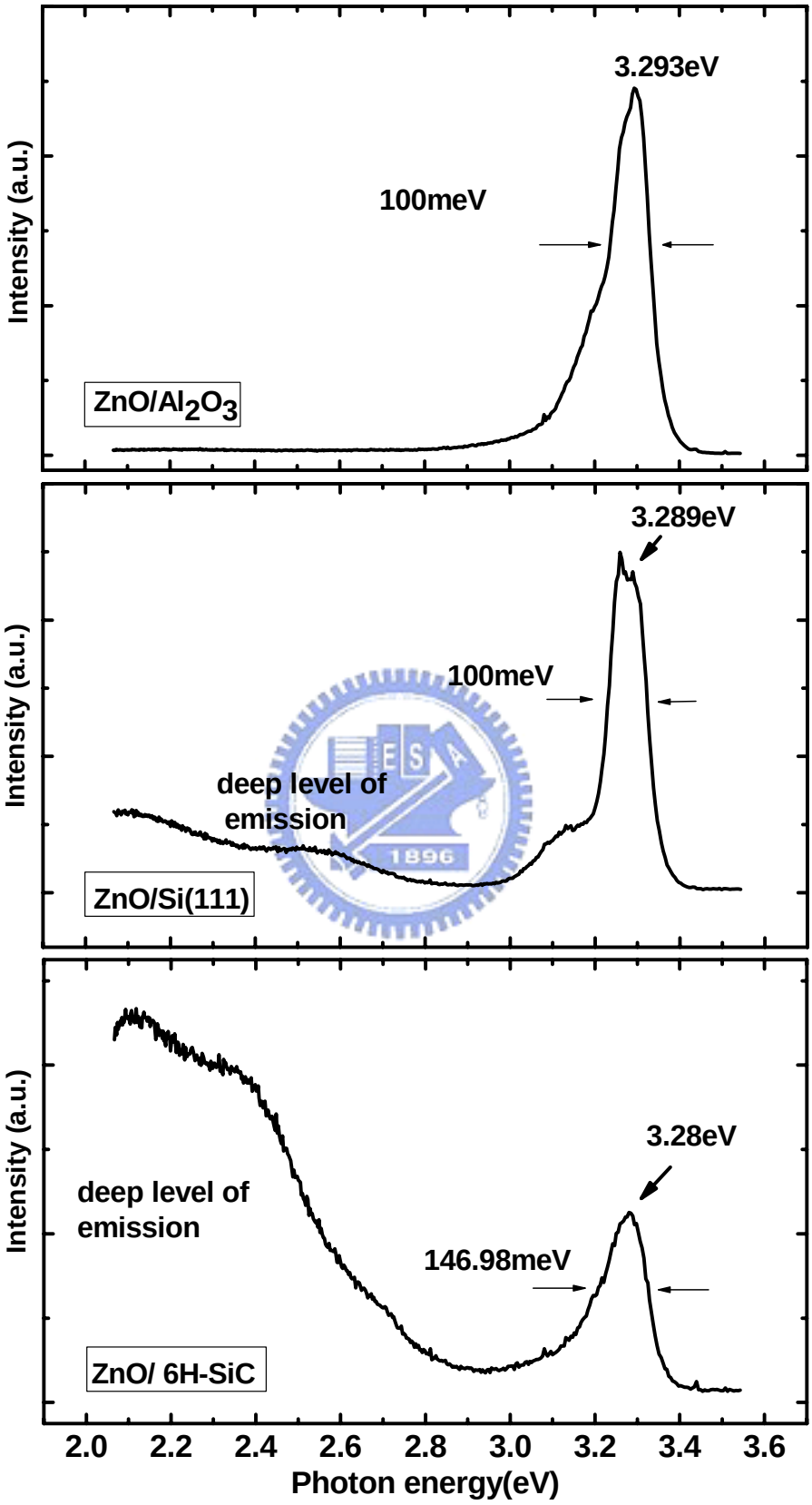

Fig. 4-11 The RT PL spectra of the ZnO/Al_2O_3, ZnO/Si (111) and ZnO/SiC samples

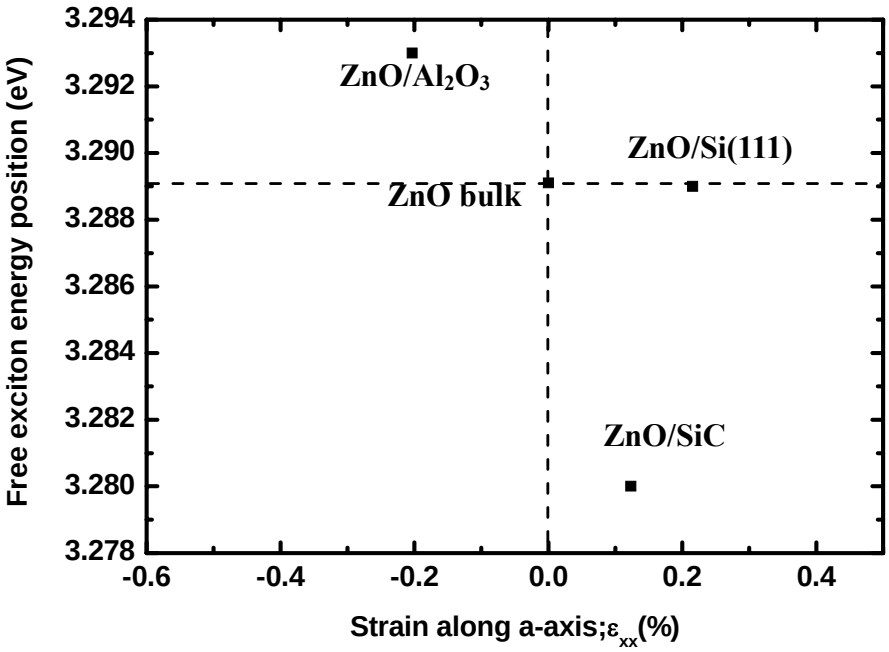

Fig. 4-12 Exciton energies of ZnO layers as a function of strain along the a axis are plotted.

4.3 Stimulated emission and Optical gain in ZnO epilayers

In this section, we use Nd:YVO_4 laser to pump the ZnO/Al_2O_3 sample and observe the stimulated emission. We vary the excitation density to calculate the threshold excitation density for the inelastic ex-ex scattering and the EHP state. With the variable strip length method, we measure the optical gain at different excitation densities.

4.3.1 Photoluminescence spectra with Nd: YVO_4 laser under various excitation densities at RT

For high excitation measurements we used a Nd: YVO_4 laser providing pulses with duration of 500 ps at a frequency of 1 kHZ. The output of Nd: YVO_4 laser at 355 nm was focused on the sample surface using a cylindrical len to form a rectangular stripe of $\ell \times 145.08\ \mu m^2$. As shown in the inset of Fig. 4-13, the excited area has a length ℓ which is determined by a fixed slit and a movable knife edge. To confirm the uniformity of the laser beam, we used a knife to adjust the length of the laser beam. Fig. 4-13 shows the excitation pumping density of the excited area extends uniformly. We therefore set the fixed slit width of 300 μm to limit the uniform pump range.

Fig. 4-14 shows normalized emission spectra from the edge of a 1.56 μm thick ZnO epilayer for a range of excitation intensities at RT. As the excitation intensity increases above 4.6 MW/cm^2, a sharp stimulated emission peak emerges at 3.15 eV and grows superlinearly. With further increase of excitation intensity above 9.2 MW/ cm^2 a second peak emerges at 3.13 eV. This peak broadens and shifts to lower energy as the excitation intensity increases.

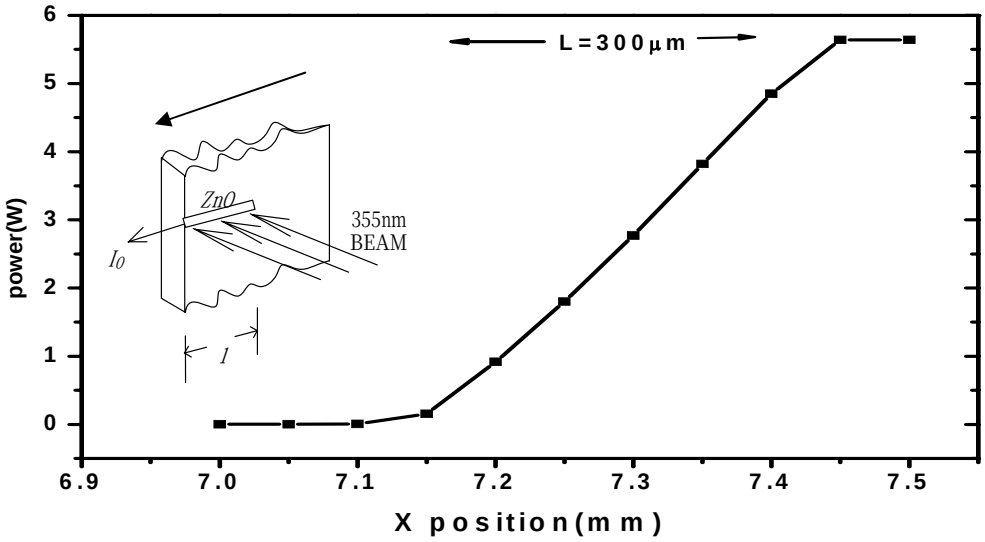

Fig. 4-13 The inset shows the method by which the crystal is excited and the amplified light (I_o) is detected.

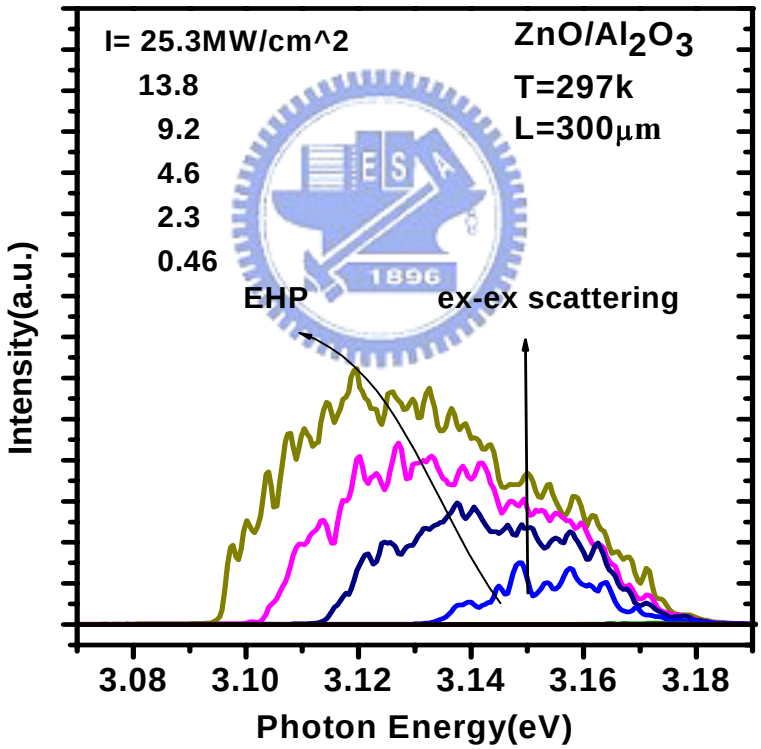

Fig. 4-14 RT PL spectra under various excitation densities show the inelastic ex-ex scattering induced stimulated emission.

Fig. 4-15 shows the spectral emission intensity versus the excitation density for the inelastic ex-ex scattering and the EHP state where the threshold excitation density is given by 4.585 MW/cm^2, 8.45 MW/cm^2, respectively. Fig. 4-15(a) shows the intensity of emission was saturated where the excitation density was above 13.8

MW/cm^2. The power dependence of the luminescence can be described by an I~L^k law, where I is the luminescence intensity and L is the excitation laser intensity, K is a coefficient. For the inelastic ex-ex scattering (3.15 eV) and the EHP state, the coefficients K are 2.047 and 2.6, respectively. The coefficient K which is larger than 1 means the luminescence intensity is superlinear with the excitation density, and the radiation is not spontaneous emission but stimulated emission.

The emission mechanisms of II–VI compounds under high excitation have been studied [31],[32]. As the excitation intensity increases, exciton density becomes sufficiently high to cause interaction with each other. In the intermediate density regime, biexciton, exciton–exciton, and exciton–carrier emissions may be observed. Biexcitonic emission is only observed at cryogenic temperatures.

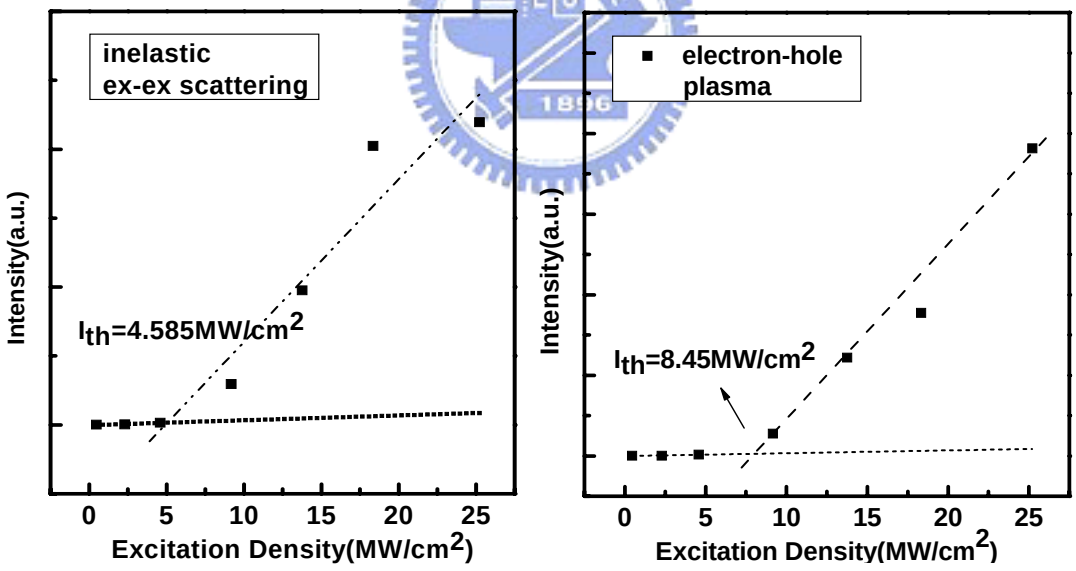

Fig. 4-15 The spectral emission intensity versus the excitation density for (a) the inelastic ex-ex scattering (b) the EHP state.

At higher temperatures exciton ionization increases the free carrier density and an increasing probability of exciton–carrier emission. At very high excitation density, the exciton density reaches such levels that excitons overlap. The superlinear increase of the emission intensity and the sharpening of the emission peak

with increasing excitation above a threshold indicate the typical nature of a stimulated emission. Using the Debye-Huckel screening theory, the Mott density in ZnO at RT is given by [33]

$$n_{\mathrm{M}} = \frac{K_{\mathrm{B}}T}{2a_{\mathrm{B}}^{3}E_{\mathrm{B}}^{\mathrm{ex}}} \sim 3.7\times10^{19}\,\mathrm{cm}^{-3}, \tag{4-2}$$

where a_{B}=18Å is the exciton Bohr radius and $E_{\mathrm{B}}^{\mathrm{ex}}$ is the exciton binding energy of ZnO. The experimental observed threshold density I_{th} for inelastic ex-ex scattering and EHP are 4.585 M W/cm^2 and 8.45 M W/cm^2; the corresponding electron-hole pair density created by a laser beam are calculated to be 7.18 X 10^{18} cm^{-3} and 1.32 X 10^{19} cm^{-3}, respectively. The former is close to the calculated Mott density and the later is larger.

$$n_{M} = \frac{(\#\ \text{of injected phtons per second})\times(\text{carrier life time})}{\text{volume}}$$

$$\mathrm{I_{th}} = 4.585\mathrm{MW/cm^2} = \left(\frac{4.585\times10^{6}}{\left(\frac{1240}{355}\times1.6\times10^{-19}\right)\times\left(0.0571\times10^{-4}\right)}\times20\times10^{-12}\right)$$

$$\sim 2.872\times10^{19}\,\mathrm{cm}^{-3}$$

$$\mathrm{I_{th}} = 8.45\mathrm{MW/cm^2} = \left(\frac{8.45\times10^{-6}}{\left(\frac{1240}{355}\times1.6\times10^{-19}\right)\times\left(0.0571\times10^{-4}\right)}\times20\times10^{-12}\right)$$

$$\sim 5.28\times10^{19}\,\mathrm{cm}^{-3} \tag{4-3}$$

where the carrier life time is 20ps [34] and the diffusion length is 57.1nm [35].

In line with the previous stimulated emission from ZnO at RT the energy position of sharp emission peak is found to be in accordance with that expected from an inelastic collision between excitons. The result of such a collision is an exciton

being excited into a higher state (n=2,3,4,….,∞), and a photon with energy given by [3]

$$P_n = E_{ex} - E_b^{ex}\left(1 - \frac{1}{n^2}\right) - \frac{3}{2}kT, \qquad n = 2,3,4,\ldots\infty \tag{4-4}$$

where E_{ex} is the free exciton emission energy, E_b^{ex} is the binding energy of the exciton, n is the quantum number of the envelope function, and kT is the thermal energy. According to (4-4),

$$P_\infty = 3.293 - 0.06\left(1 - \frac{1}{\infty^2}\right) - 0.0387 = 3.1943 \text{ eV}$$

$$> 3.15 \text{ eV} \tag{4- 5}$$

the inelastic ex-ex scattering would lie in 3.1943eV, [see Fig. 4-10] which is larger than the experimental data, 3.15eV. The pumping laser would induce heat on the surface of the sample and enlarge the thermal energy would enlarge $\frac{3}{2}kT$. Thus P_∞ would red shift to the small energy.

4.3.2 Stimulated emission spectra for various excitation stripe lengths at RT

By using the variable stripe length method (VSLM) [36], we measured the optical gain spectrum of these ZnO epilayers. Fig. 4-16(A) shows the stimulated emission spectra with excitation density neat I_{th} (I_{pump}=9.19MW/cm^2) for various excitation stripe lengths and Fig. 4-15(B) is under I_{pump}=25.3MW/cm^2. The emission spectrum is a broad asymmetric band, which is red shifted versus the increase of the excitation length ℓ. The sharp increase of the emission intensity with excitation length indicates the presence of optical gain. Based on the one-dimensional optical amplifier mode for an excited media, the spectra were analyzed by fitting to the equation (4-6) where be derived in chapter 2.

$$I(\ell, h\upsilon) = \frac{I_{spont}(h\upsilon)A}{g'(h\upsilon)}\left(e^{g'(h\upsilon)\ell} - 1\right) \qquad (4\text{-}6)$$

With increasing of the pumping stripe length, the position of the emission peak red shift. Under higher pumping density, the position of the emission peak red shift more. According to the report of Yefan Chen's et. al [13], a redshift was observed when the excitation exceeds 220kW/cm^2, which gives a sign of the emergence of EHP. However, it may be also due to the quality of the ZnO thin film [37]. Good quality ZnO thin films would have fewer defects than poor quality ones. In this way, near band edge emission of the photoluminescence would be narrower and the intensity of the donor-acceptor pair would be smaller. In the absorption coefficient versus photon energy (Fig. 4-16), the absorption coefficient of the thin films with good quality (α) would increase more steeply than that of the thin films with poor quality (α'). Thus absorption coefficient of thin films with poor quality would have band tailing. The optical gain recording by VSLM was net optical gain g' = ($g-\alpha$) or ($g-\alpha$'). As the excitation length is small, the multiplier $\alpha'\ell$ is smaller for large photon energy, thus the intensity is higher. However, with the longer excitation length, the multiplier $\alpha'\ell$ is larger for large photon energy so that the photoluminescence would red shift.

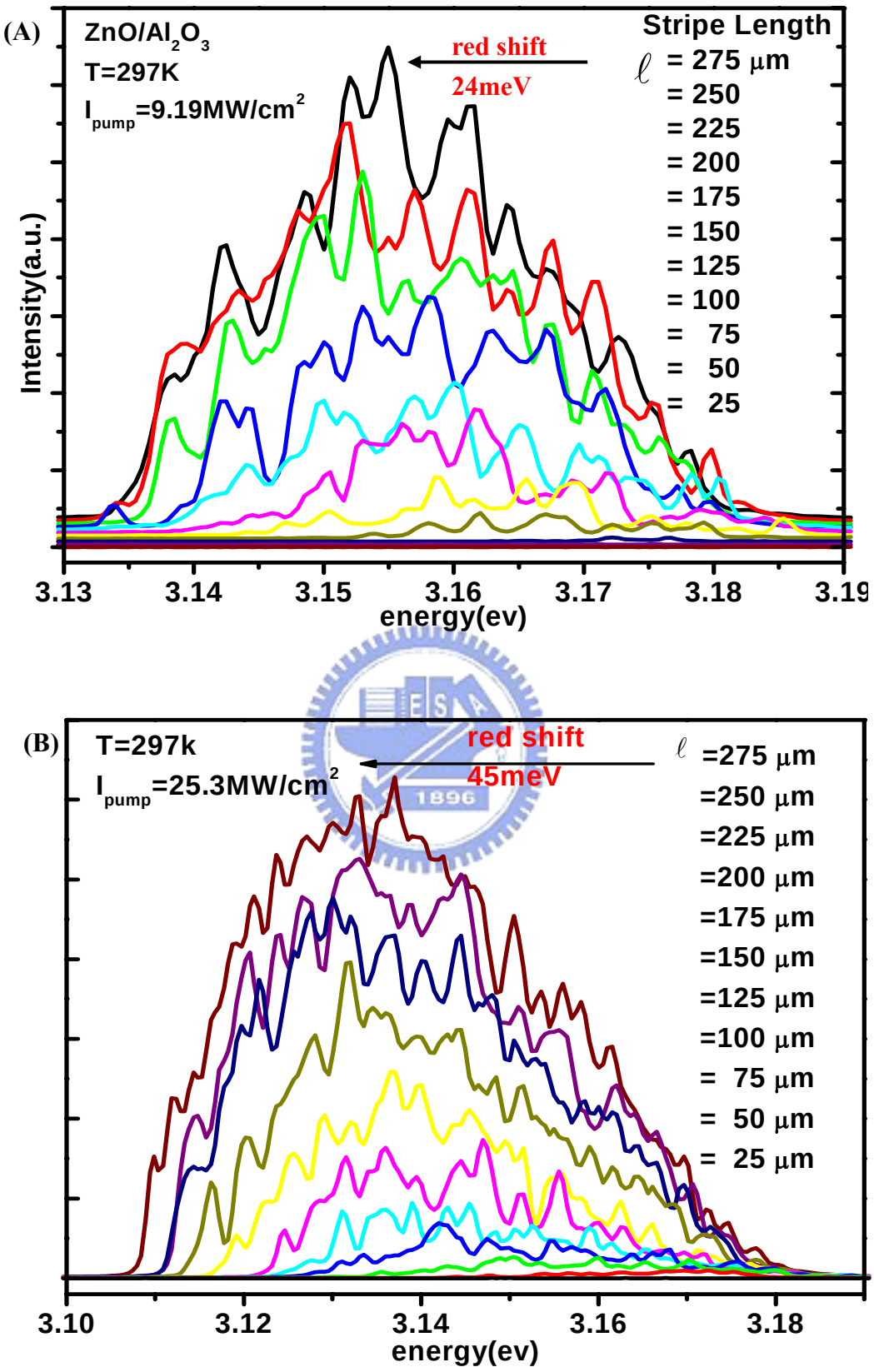

Fig. 4-16 Stimulated emission spectra for various excitation stripe lengths at RT. I_{pump}= (A) 9.19 MW/cm^2 (B) 25.3 MW/cm^2

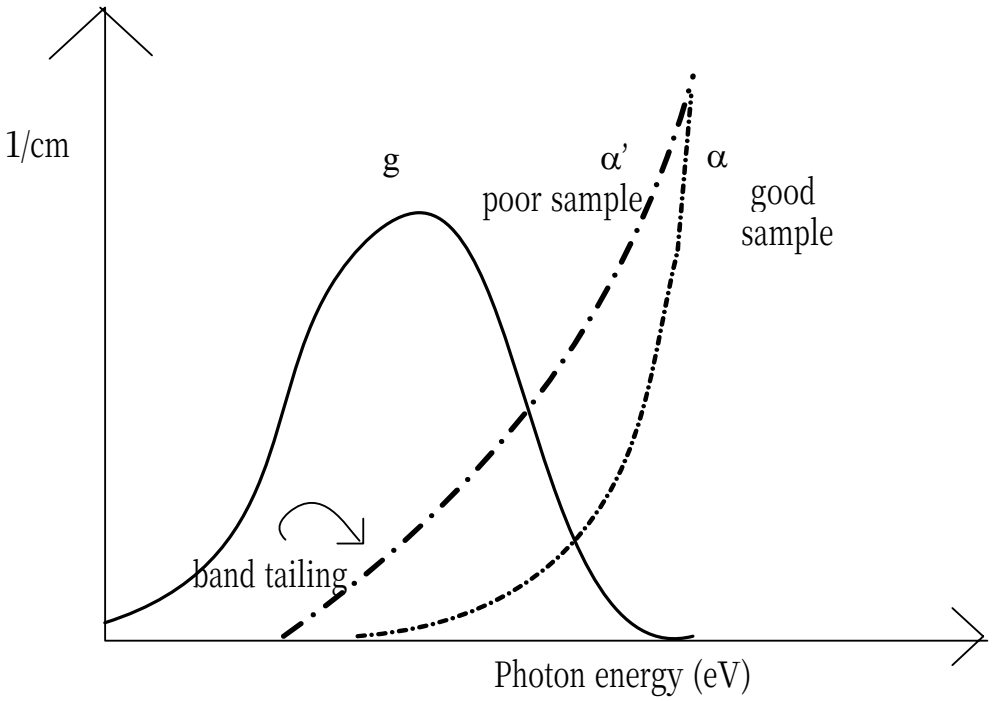

Fig.4-17 absorption coefficient versus photon energy for good quality (α) and poor quality of ZnO thin films (α').

4.3.3 Optical gain spectrum of a ZnO epilayer at various excitation densities

Fig. 4-18 shows the variation of output intensity with increasing length for different photon energy where the excitation density is 25.3 MW/cm^2. Intensity versus excitation length varies according to (4-6). The gain coefficient g determinates the direction of the concave of the curve. As g is smaller than 0, the concave would face toward downward. In the other way, the concave of the curve would face upward as g is larger than 0. As g is approximate to 0, the curve would be linear-like. The evaluated optical gain as a function of photon energy is plotted in Fig. 4-19. The excitation density increases from Fig. 4-18(c) to Fig. 4-18(a) where a dominant peak in the curve shifts from 3.138 eV to 3.15 eV. The dominant peak was

attributed to the EHP state because it would blue shift with excitation densities. On the right of the dominant peak there exists a shoulder which is attributed to the inelastic ex-ex scattering. At an excitation density of 9.2 MW/cm^2, the peak gain is about 180 cm^{-1} with a redshift about 16meV as the excitation density becomes 13.8 MW/cm^2. The peak gain seems smaller than that reported by P. Yu and co-workers [2]. This results from different pumping conditions as well as the lack of light confinement in our samples. The peak gain seems smaller than that reported by Y. F. Chen [13], too. This is induced by the quality of the ZnO thin films.

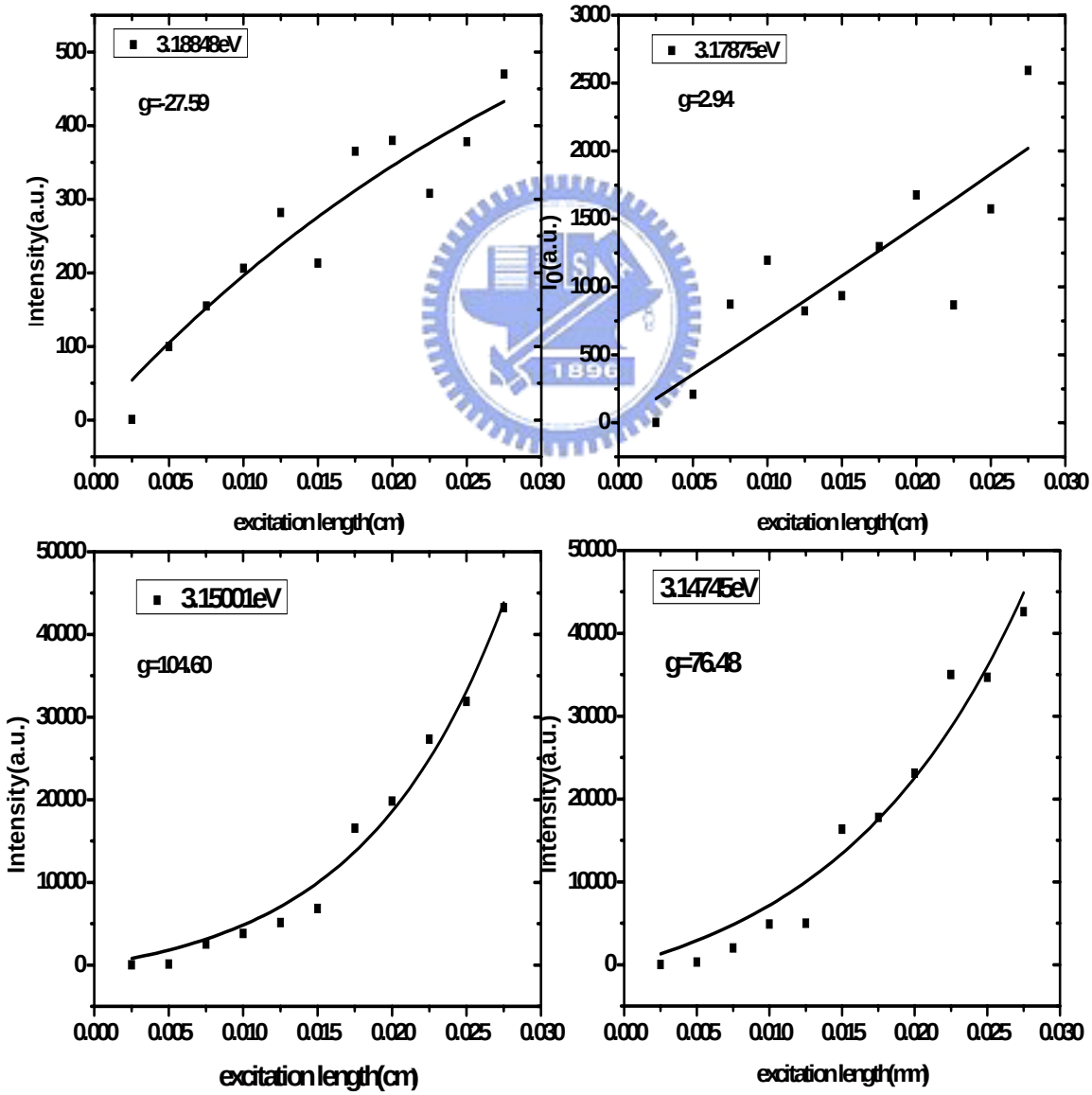

Fig. 4-18 A set of the variation of light output with length of excited region for excitation density=25.3 MW/cm^2.

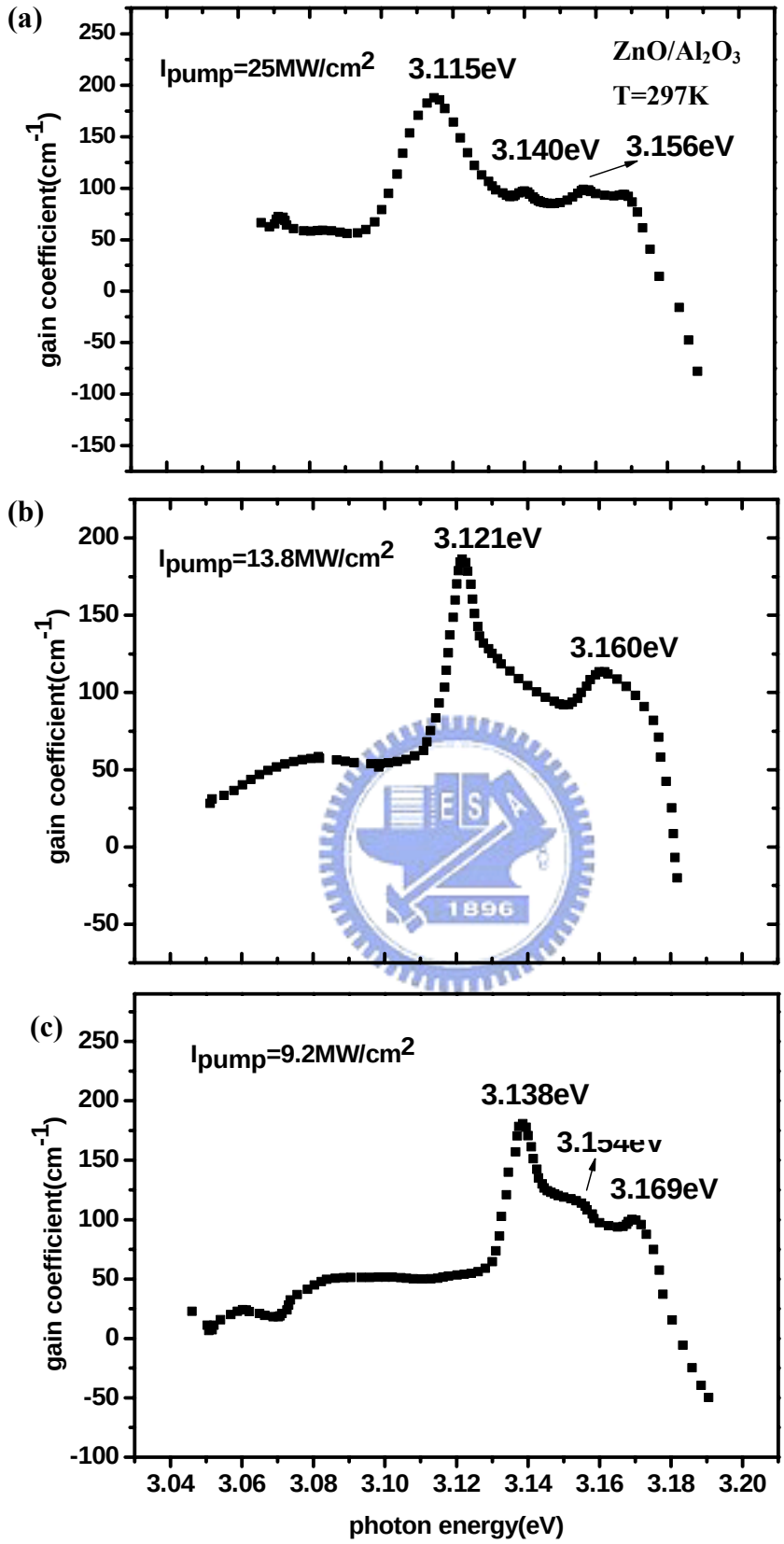

Fig. 4-19 Optical gain spectrum of a ZnO epilayer under various excitation density at RT

Chapter 5
Conclusion and Perspective

5.1 Conclusions

From the RHEED observation and ω–rocking curve, we found qualities of ZnO/Al_2O_3 and ZnO/SiC are better. Phi scans for (202) peaks of three samples indicate six-fold symmetry and epitaxial growth of the ZnO thin films onto Al_2O_3 and SiC except Si (111). We have investigated X ray ω-2θ scan for (002) and (110) reflections to determine in-plane and out of the plane lattice constants of ZnO thin films on different substrates. With room-temperature PL spectra of ZnO epilayers grown on Al_2O_3, Si (111) and SiC substrates, we can derive the stress states in films. The thermal stress can also play a key role in deciding the residual strain in film.

Beside, we report RT stimulated emission and optical gain spectra of high-quality ZnO epilayers on Al_2O_3. We found that the inelastic ex-ex scattering dominantly contributes to the optical gain at excitation densities, 4.585 MW/cm^2 and the EHP state at excitation densities, 8.45MW/cm^2. Maximum gain of 187 cm^{-1} at the excitation density of 25 MW/cm^2 is obtained. With increasing excitation, density contribution from the EHP state gradually takes over at the lower energy side in the optical gain spectrum. This work clearly shows that without quantum or light confinement, excitons play the main role in the emission processes of ZnO at RT in both low and intermediate excitation regimes.

5.2 Perspective

In our research, we have derived the relationship between the photoluminescence properties and the biaxial strain of the epilayer. It could be a tool

to diagnose the strain of the ZnO epilayer substrate. However, the strain can be relaxed by the thickness of the ZnO thin films, even it exists a critical thickness to release the strain completely. In the future, it may be put to the proof about the strain and the thickness.

There is large advantage in the growth of ZnO on Si because of large scale integration using natured Si technology. However, among three samples, quality of the ZnO/Si (111) sample is poor. According to Y. –Z. Yoo et. al. report [38], deposition of ZnO onto Si causes the formation of an amorphous interface (SiO_2) between the film and the substrate, which leads to the poor quality of the ZnO films. It is reasonable to use a buffer layer to prevent SiO_2 formation. For the growth of ZnO on Si, a buffer with the same hexagonal symmetry as ZnO is desirable to minimize the structural mismatch, like wurtzite ZnS.

Although different optical pumping conditions could be a reason for the observed discrepancy, the different crystal properties of the epilayers play a critical role in lasing mechanisms. The structural defects result in numerous optical losses and thus a high threshold. Thus, different samples may have different pumping threshold. Therefore, it can study the relationship between the crystalline quality and the properties of the stimulated emission.

References

[1] Yefan Chen, D. M. Bagnall, H. Ko, K. Park, K. Hiraga, Z. Zhu, and T. Yao, J. Appl. Phys. 84 (1998) 3912.

[2] P. Yu, Z. K. Tang, G. L. Wong, M. Kawasaki, A. Ohtomo, H. Koinuma, and Y. Segawa, in *23rd International Conference on the Physics of Semiconductors,* edited by M. Scheffler and R. Zimmermann (World Scientific, Singapore, 1996), p. 1453; Z. K. Tang, G. K. L. Wong, P. Yu, M. Kawasaki, A. Ohtomo, H. Koinuma, and Y. Segawa, Appl. Phys. Lett. 72 (1998) 2466.

[3] D. M. Bagnall, Y. F. Chen, Z. Zhu, T. Yao, S. Koyama, M.Y. Shen and T. Goto, Appl. Phys. Lett. 70 (1997) 2230.

[4] D. C. Look, Materials Science and Engineering B 80 (2001) 383.

[5] M. Zamfirescu, A. Kavokin, B. Gil, G. Malpuech, and M. Kaliteevski, Phys. Rev. B 65 (2002) 161205.

[6] Y. Chen, H. Ko, S. Hong, and T. Yao, Appl. Phys. Lett. 76 (2000) 559.

[7] P. Fons, K. Iwata, S. Niki, A. Yamasa, and K. Matsubara, J. Cryst. Growth 201 (1999) 627.

[8] A. Ohtomo, K. Tamura, K. Saikusa, K. Takahashi, T. Makino, Y. Segawa, H. Koinuma, and M. Kawasaki, App. Phys. Lett. 75 (1999) 2635.

[9] P. Yu, Z. K. Tang, G. K. L. Wong, M. Kawasaki, A. Ohtomo, H. Koinuma, and Y. Segawa, J. Cryst. Growth 184 (1998) 601.

[10] Hung-Yu Lin, “The growth and Optical Properties of ZnO Thin Films by Laser Molecular Beam Epitaxy”, a thesis for the degree of master, Institute of Electro-Optical Engineering of National Chiao Tung University, 2003.

[11] A. B. M. Almamun Ashrafi, Naguyen Thanh Binh, Bao-ping Zhang, and Yusaburo Segawa, Appl. Phys. Lett. 84 (2004) 2814.

[12] D. G. Zhao, S. J. Xu, M. H. Sie, S. Y. Tong and Hui Yang, Appl. Phys. Lett. 83 (2003) 677.

[13] Yefan Chen, N. T. Tuan, Yusaburo Segawa, Hang-ju Ko, Soon-Ku Hong and Takafumi Yao, Appl. Phys. Lett. 78 (2001) 1469.

[14] R. Paszkiewicz, B. Paszkiewicz, R. Korbutowicz, J. Kozlowski, M. Tlacazala, L. Bryja, R. Kudrawiec, and J. Misiewicz, Cryst. Res. Technol. 36 (2001) 971.

[15] T. H. K. Barron and G. K. White, "Heat Capacity and Thermal Expansion at Low Temperature", Kluwer Academic/Plenum Publishers.

[16] Charles Kittel, "*Introduction to Solid State Physics*", 7th edition, p. 561.

[17] Wolfgang Braun, "*Applied RHEED: reflection-high energy electron diffraction during crystal growth*", Springer tracts in modern physics Vol. 154 (1999), p. 13-p. 15.

[18] Jacques l. Pankove, "*Optical Processes in Semiconductors*", p. 14, p. 16-18 and p. 214.

[19] C. F. Klingshirn, "*Semiconductor Optics*", Springer (1997), p. 241.

[20] Yefan Chen, Darren Bagnall and Takafumi Yao, Materials Science and Engineering B75 (2000) 190–198.

[21] Yefan Chen, Hang-jun Koh, Soon-ku Hong, Takafumi Yao and Yusaburo Segawa, J. Crystal Growth 214/215 (2000) 87.

[22] Charles Kittel, "*Introduction to Solid State Physics*", 7th edition, p. 555.

[23] T. M. Parker, N. G. Condon, R. Lindsay, F. M. Leibsile, G. Thornton, Surf. Sci. 415 (1998) L1046.

[24] S. H. Overbury, P. V. Radulovic, S. Thevuthasan, G. S. Herman, M. A. Henderson, C. H. F. Peden, Surf. Sci. 410 (1998) 105.

[25] S. C. Chang, P. Mark, Surf. Sci. 46 (1974) 293.

[26] R. W. Nosker, P. Mark, J. D. Levine, Surf. Sci. 19 (1970) 291.

[27] Ashrafi ABMA, Zhang BP, Binh NT, Wakatsuki K, and Segawa Y, Jan. J. Appl. Phys. Part 1-Regular Papers Short Notes & Review Papers 43 (2004) 1114.

[28] Craciun V, Singh RK, Perriere J, J. Electrochem Soc. 147 (2000) 1077.

[29] H. Lahreche, P. Vennegues, O. Tottereau, M. Laugt, P. Lotenzine, M. Lerous, B. Beaumont, and P. Gibart, J. Crystal Growth 217 (2000) 13.

[30] B. P. Zhang, N. T. Binh, Y. Segawa, Y. Kashiwaba and K. Haga, Appl. Phys. Lett. 84 (2004) 586.

[31] D. M. Bagnall,C. Klingshirn, H. Kalt, M. Umlauff, W. Petri, F. A. Majumder, S. V. Bogdanov, W. Langbein, M. Grun, M. Hetterich, K. P. Geyzers, M. Heuken, A. Naumov, H. Stanzl, and W. Gebhardt, J. Crystal Growth 138 (1994) 786.

[32] C. Klingshirn, H. Kalt, M. Umlauff, W. Petri, F. A. Majumder, S. V. Bogdanov, W. Langbein, M. Grun, M. Hetterich, K. P. Geyzers, M. Heuken, A. Naumov, H. Stanzl, and W. Gebhardt, J. Crystal Growth 138 (1994) 786.

[33] C. F. Klingshirn, *Semiconductor Optics* (Springer-Verlag, Berlin, 1995), p. 307.

[34] T. Koida, S. F. Chichibu, A. Uedono, T. Sota and A. Tsukazaki and M. Kawasaki, Appl. Phys. Lett. 84 (2004) 1079.

[35] J. F. Muth, R. M. Kolbas, A. K. Sharma, S. Oktyabrsky, and J. Narayan J. of Appl. Phys. 85 (1999) 7884.

[36] K. L. Shaklee, R. E. Nahory, R. F. Leheny, J. Lumin. 7 (1973) 284.

[37] S. Hess, R. A. Taylor, and J. F. Ryan, Appl. Phys. Lett. 73 (1998) 199.

[38] Y.-Z. Yoo, T. Sekiguchi, T. Chikyow, M. Kawasaki, T. Onuma, S. F. Chichibu, J. H. Song and H. Koinuma, Appl. Phys. Lett. 84 (2004) 502.